OPTIMIZING PULSED EDDY CURRENT FOR INSPECTION OF SECOND LAYER WING STRUCTURE

L'OPTIMISATION DES COURANTS DE FOUCAULT PULSÉS POUR L'INSPECTION DE LA DEUXIÈME COUCHE STRUCTURALE D'UNE AILE D'AVION

A Thesis Submitted to the Division of Graduate Studies
of the Royal Military College of Canada
by

Dennis Morgan Butt, B.Eng.
Captain

In Partial Fulfillment of the Requirements for the Degree of
Master of Applied Science in Chemical and Materials Engineering

May 2016

© This thesis may be used within the Department of National Defence but copyright for open publication remains the property of the author.

ROYAL MILITARY COLLEGE OF CANADA
COLLÈGE MILITAIRE ROYAL DU CANADA

DIVISION OF GRADUATE STUDIES AND RESEARCH
DIVISION DES ÉTUDES SUPÉRIEURES ET DE LA RECHERCHE

This is to certify that the thesis prepared by / Ceci certifie que la thèse rédigée par

Dennis Morgan Butt

entitled / intitulée

OPTIMIZING PULSED EDDY CURRENT FOR INSPECTION OF SECOND LAYER WING STRUCTURE /
L'OPTIMISATION DES COURANTS DE FOUCAULT PULSÉS POUR L'INSPECTION DE LA DEUXIÈME COUCHE STRUCTURALE D'UNE AILE D'AVION

complies with the Royal Military College of Canada regulations and that it meets the accepted standards of the Graduate School with respect to quality, and, in the case of a doctoral thesis, originality / satisfait aux règlements du Collège militaire royal du Canada et qu'elle respecte les normes acceptées par la Faculté des études supérieures quant à la qualité et, dans le cas d'une thèse de doctorat, l'originalité

for the degree of / pour le diplôme de

Master of Applied Science / Maîtrise en Science Appliquée

Signed by the final examining committee: /
Signée par les membres du comité examinateur de la soutenance de thèse

_____, Chair / Président

_____, External Examiner / Examinateur externe

_____, Main Supervisor / Directeur de thèse principal

Approved by the Head of Department : /
Approuvée par le Directeur du Département : _____ Date: _____

To the Librarian: This thesis is not to be regarded as classified. /
Au Bibliothécaire: Cette thèse n'est pas considérée comme à publication restreinte.

_____
Main Supervisor / Directeur de thèse principal

Acknowledgements

I would like to thank Dr. Thomas Krause, my thesis supervisor, for his guidance and patience throughout the last two years. His dedication to the field of non-destructive testing (NDT) in combination with his instruction and feedback were instrumental to the success of this thesis.

I would also like to thank Dr. Ross Underhill for his assistance with building probes and circuit boards, designing LabVIEW software interfaces and programming computer algorithms. This thesis work would not have been a success without the insights he provided from his vast knowledge of statistical methods.

Additionally, I would like to thank Major Peter Horan from the Directorate of Technical Airworthiness and Engineering Support (DTAES) and Captain Colette Stott from the Aerospace and Telecommunications Engineering Support Squadron (ATESS) for their assistance with funding conferences and procurement of test samples, along with providing technical advice as NDT subject matter experts.

Finally, I would like to thank my wife Weronika, my daughter Walentyna and my soon-to-be-born son Dominik for their patience and understanding throughout the past two years. Your love and support has helped me to endure numerous challenges and I could not have succeeded in this venture without all three of you by my side.

Abstract

A thesis completed by Butt, Dennis Morgan, in partial fulfillment of the requirements for a Master of Applied Science in Chemical and Materials Engineering form the Royal Military College of Canada on the 27th of May 2016 on *OPTIMIZING PULSED EDDY CURRENT FOR INSPECTION OF SECOND LAYER WING STRUCTURE*, under the direction of Dr. Thomas Krause.

Due to cyclic loading conditions experienced during typical aircraft operation, ageing aircraft are susceptible to fatigue cracks at bolt hole locations in multi-layer aluminum wing lap-joints. Inspection from the top layer, without fastener removal, is desired in order to minimize aircraft downtime, while reducing the risk of collateral damage. The ability to detect second layer cracks without fastener removal has been demonstrated using a pulsed eddy current (PEC) technique. This technique takes advantage of a probe design, which utilizes the ferrous fastener as a flux conduit to induce eddy currents in the surrounding structure. Differentially connected pick-up coils sense eddy current response changes due to the presence of a crack. The differential signal response is analyzed using a modified principal components analysis (MPCA). These MPCA scores are then processed using a cluster analysis to identify the presence of cracks. Probe design features, data acquisition system parameters and signal post-processing can each have a strong impact on crack detection. Physical probe configurations and signal analysis processes, used to enhance the PEC system for detection of cracks in CP-140 Aurora (P-3 Orion) lap-joint structures, are investigated and an enhanced probe design is identified. Effective results are obtained using the cluster analysis approach for single sample cases. However, problems arise when the technique is applied concurrently to multiple lap-joint samples. The development of an expanded analysis approach for applicability to multiple CP-140 Aurora (P-3 Orion) lap-joint samples is investigated and detection results are presented for both the single sample and combined sample scenarios. The cluster analysis methodology is further limited by the fact that a number of representative blank fastener signals are required in order to perform classification of the data. Using the smallest half volume (SHV) analysis methodology, a series of simulations are conducted in order to demonstrate the ability of the SHV method to be used for blind outlier detection without having to obtain representative blank fastener signals.

Résumé

Thèse complétée par Butt, Dennis Morgan, pour la satisfaction partielle d'une maîtrise ès sciences appliquées en génie chimique et des matériaux du Collège militaire royal du Canada ce 27 mai 2016 sur *L'OPTIMISATION DES COURANTS DE FOUCAULT PULSÉS POUR L'INSPECTION DE LA DEUXIÈME COUCHE STRUCTURALE D'UNE AILE D'AVION,* sous la supervision directe du Dr Thomas Krause.

Vu la présence de conditions cycliques de chargement durant une opération aérienne normale, les avions vieillissants sont susceptibles d'avoir des fissures, dues à la fatigue, présentes aux sites des trous de boulons parmi les joints de recouvrements des couches d'aluminium de leurs ailes. Une inspection de la couche du dessus, sans en démonter les attaches, est la méthode désirée afin de réduire le temps d'immobilisation de l'avion ainsi que le risque de dommages collatéraux. La méthode des courants de Foucault pulsés (CFP) a la capacité de permettre la détection de fissures dans la deuxième couche structurale sans en démonter les attaches. Cette méthode prend avantage d'un modèle de sondes qui utilisent les attaches en fer en tant que conduits afin de provoquer des courants de Foucault dans la structure entourant celles-ci. Des bobines de prise connectées de façon différentielle détectent les variations des réponses des courants de Foucault causées par la présence de fissures. Les réponses des signaux différentiels sont analysées grâce à une analyse modifiée en composantes principales (AMCP). Les résultats de l'AMCP sont traités selon une analyse par grappes afin de permettre l'identification de fissures. Les caractéristiques de la conception des sondes, les paramètres des systèmes d'acquisition de données et le traitement des signaux peuvent chacun en soi avoir un grand impact sur la détection de fissures. Les configurations physiques des sondes ainsi que les procédures de traitement des signaux, utilisées afin d'optimiser le système des CFP de détection de fissures dans les structures des joints de recouvrements des CP-140 Aurora (P-3 Orion), sont examinées et une configuration améliorée pour les sondes est identifiée. Des résultats efficaces pour les échantillons uniques sont obtenus grâce à une analyse de grappes. Par contre, des difficultés se présentent lorsque cette technique est utilisée parallèlement sur plusieurs échantillons de joints de recouvrements. Le développement d'une méthode d'analyse étendue pour une application sur plusieurs joints de recouvrements des CP-140 Aurora (P-3 Orion) est examiné et les résultats des détections pour des échantillons uniques et multiples sont présentés. La méthode d'analyse de grappes est davantage limitée par le fait qu'un certain nombre de signaux représentatifs d'attaches sans

défaut est requis afin d'accomplir la classification des résultats. Une série de simulations est réalisée en utilisant la méthode d'analyse du plus petit demi-volume (PPDV) afin de démontrer la capacité de détection de cette méthode même en l'absence de signaux représentatifs d'attaches sans défaut.

Table of Contents

Acknowledgements iii
Abstract iv
Résumé v
List of Tables x
List of Figures xi
List of Abbreviations xiii
1. Introduction 1
1.1 Background 1
1.2 Eddy Current Testing 3
1.3 Outlier Detection 5
1.4 Objective 7
1.5 Thesis Scope and Methodology 7
2. Theory 11
2.1 General 11
2.2 Maxwell's Equations 11
2.3 Electromagnetic Diffusion Equations 13
2.4 Skin Depth Theory 14
2.5 Eddy Current Generation 14
2.6 Equivalent Circuit Models 15
2.7 Modified Principal Components Analysis (MPCA) 20
2.8 Cluster Analysis Method 22
2.9 Robust Statistics Method 23
2.10 Randomly Generating Covariance Matrices 24
3. Literature Review 26
3.1 General 26
3.2 Analytical Work 26
3.3 Detecting Defects in Multi-Layer Aircraft Structures 27
3.4 Detecting Defects in the Presence of Ferrous Fasteners 29
3.5 Multivariable Outlier Detection 32

4. Experimental Technique 34
4.1 General 34
4.2 Probe Enhancement 34
4.3 Data Acquisition Equipment 36
4.4 Operational Amplifier Circuit Evaluation 36
4.5 NAVAIR Sample Series Description 39
4.6 Probe Alignment 44
5. Signal Processing and Analysis 46
5.1 General 46
5.2 Signal Gating 46
5.3 Cluster Analysis 48
5.4 Removing Shifts Due to Environmental Factors 49
5.5 Repeat Measurement Effects 50
5.6 Fastener Proximity to the Lap-Joint Edge 52
5.7 Robust Statistics Simulations 54
6. Results 56
6.1 General 56
6.2 Probe Enhancement Results 56
6.3 Measurement Detection Results 58
6.3.1 Single Sample Detection Results 58
6.3.2 Combined Sample Detection Results 59
6.4 Simulation Detection Results 59
6.4.1 Results Obtained with Known Blanks 60
6.4.2 Blind Detection Results 60
7. Discussion 62
7.1 Probe Enhancement 62
7.2 Selecting an Analysis Method 62
7.3 Determining Detectable Flaw Size and False Call Rate 65
8. Summary and Future Work 67
8.1 Summary 67
8.2 Future Work 69

References 70
Appendix A 74
Curriculum Vitae 80

List of Tables

Table 1: Description of variables for the circuit diagram shown in Figure 6 17
Table 2: Detailed probe specifications for the four PEC probes evaluated 35
Table 3: Standard 22 notch sizes, locations and orientations 40
Table 4: Standard 23 notch sizes, locations and orientations 41
Table 5: Standard 24 notch sizes, locations and orientations 41
Table 6: Standard 25 notch sizes, locations and orientations 42
Table 7: Standard 26 notch sizes, locations and orientations 42
Table 8: Standard 28 notch sizes, locations and orientations 43
Table 9: Standard 32 notch sizes, locations and orientations 43
Table 10: P-3 Orion sample series blank fastener locations 44
Table 11: P-3 Orion sample series top and bottom layer thickness with interlayer gap (uncertainties are estimated as being to within stated significant figures) 44
Table 12: Overall detection results for Probes 1, 2, 3 and 4 58
Table 13: Summary of single sample detection results 58
Table 14: Summary combined sample detection results 59
Table 15: Summary of detection results for known randomly generated blanks 60
Table 16: Minimum false call rate where miss occurs 60
Table 17: Summary of detection results for SHV in the presence of outliers 61

List of Figures

Figure 1: Cross-section of a typical lap-joint configuration showing bottom-of-top layer and top-of-bottom layer cracks along with the ferrous fastener location 2

Figure 2: Typical drill bit damage incurred during removal of a steel ferrous fastener securing an aluminum lap-joint 3

Figure 3: Flow of eddy currents in typical test piece geometries indicating that eddy currents flow in a circular pattern perpendicular to the applied magnetic field 4

Figure 4: RL circuit representing a typical PEC excitation coil 15

Figure 5: Plot of the resulting transient current produced when the switch is instantaneously closed for the circuit diagram shown in Figure 4 as represented by Equation 2.23 16

Figure 6: Equivalent circuit diagram for a PEC driving coil coupled with a single pick-up coil 17

Figure 7: Typical transient current produced when the switch is instantaneously closed for the mutual inductance circuit shown in Figure 6 as represented by Equation 2.29 19

Figure 8: Graphical representation of a three-way mutual inductance relationship between a PEC driving coil, a single pick-up coil and the conductive sample being evaluated 19

Figure 9: Plot showing blank fastener scores s_2 vs. s_3 for measurements taken from three P-3 Orion samples with blank cluster, MD and a single defect identified 23

Figure 10: Three of the four probes representing varying core diameters. 5 mm (grey), 6 mm (blue) and 8 mm (red) probe configurations 35

Figure 11: Flow chart depicting the flow of information in the data acquisition process 36

Figure 12: First five eigenvectors produced from MPCA of a pick-up coil pair response signal when the driver pulse was produced using a Darlington pair based amplification circuit 37

Figure 13: Circuit diagram for PA75 dual power op-amp wired in a noninverting configuration 37

Figure 14: First five eigenvectors produced from MPCA of a pick-up coil pair response signal when the driver pulse was produced using an op-amp configured in a noninverting amplifier 38

Figure 15: Top and side view of P-3 Orion sample showing the location of top and bottom layers along with fasteners and lap-joint edge 39

Figure 16: Probe with alignment guide and sample 45

Figure 17: Raw PEC differential pick-up coil response showing the front and back end transient response along with the chosen signal gate obtained from screenshot of the LabView display .. 47

Figure 18: Raw PEC data signal showing the front end of a typical transient pick-up coil response with signal gate boundaries indicated 48

Figure 19: Plot of blank scores obtained for standards 22, 24 and 25 showing a shift in the blank clusters due to environmental factors 50

Figure 20: Plot of blank scores obtained for standards 22, 24 and 25 showing re-centered blank clusters with environmental shift removed 50

Figure 21: Plot showing an example of variation in repeat measurements due to horizontal probe off-centering 51

Figure 22: Plot showing an example of repeat measurement variation contained in s_1 only after a unitary rotation is applied 51

Figure 23: Fastener edge distance vs. s_5 for Standard 22 without edge correction 52

Figure 24: Fastener edge distance vs. s_5 for Standard 22 after edge correction 52

Figure 25: Plot of blank scores for three standards showing s_2 vs. s_3 without edge corrections 53

Figure 26: Plot of blank scores for three standards showing s_2 vs. s_3 after edge corrections 53

Figure 27: Detection rate vs. false call rate for simulations using the SHV algorithm with a data set containing 4 cracks and 40 blanks 55

Figure 28: Side-by-side comparison of notch detection results for Probes 1, 2 & 4 with a total of 25 measurements taken per fastener 57

Figure 29: Side-by-side comparison of notch detection results for Probes 3 & 4 with a total of 25 measurements taken per fastener 57

Figure 30: Fastener edge distance vs. s_2 for Standard 22 without edge correction 74

Figure 31: Fastener edge distance vs. s_2 for Standard 22 after edge correction 74

Figure 32: Fastener edge distance vs. s_3 for Standard 22 without edge correction 75

Figure 33: Fastener edge distance vs. s_3 for Standard 22 after edge correction 75

Figure 34: Fastener edge distance vs. s_4 for Standard 22 without edge correction 76

Figure 35: Fastener edge distance vs. s_4 for Standard 22 after edge correction 76

Figure 36: Plot of blank scores for three standards showing s_4 vs. s_5 without edge corrections 77

Figure 37: Plot of blank scores for three standards showing s_4 vs. s_5 after edge corrections 77

Figure 38: Plot of blank scores for three standards showing s_2 vs. s_4 without edge corrections 78

Figure 39: Plot of blank scores for three standards showing s_2 vs. s_4 after edge corrections 78

Figure 40: Plot of blank scores for three standards showing s_2 vs. s_5 without edge corrections 79

Figure 41: Plot of blank scores for three standards showing s_2 vs. s_5 after edge corrections 79

List of Abbreviations

ATESS	Aerospace and Telecommunications Engineering Support Squadron
BHEC	Bolt Hole Eddy Current
CAD	Computer-Aided Design
CFRP	Carbon Fibre-Reinforced Polymer
DAQ	Data Acquisition
EDM	Electric Discharge Machined
ET	Eddy Current Testing
FEA	Finite Element Analysis
ICA	Independent Components Analysis
NAVAIR	Naval Air Systems Command
NI	National Instruments
MCD	Minimum Covariance Determinant
MD	Mahalanobis Distance
MPCA	Modified Principal Components Analysis
MVE	Minimum Volume Ellipsoid
NDT	Non-destructive Testing
PCA	Principal Components Analysis
PEC	Pulsed Eddy Current
POD	Probability of Detection
RCAF	Royal Canadian Air Force
RHM	Resampling by Half-means
SCC	Stress Corrosion Cracking
SHV	Smallest Half Volume
SVM	Support Vector Machine

1. Introduction

1.1 Background

Reliability is defined as the probability that a system will perform its intended function for a stated period of time under specified operating conditions [1]. In order to mitigate the possibility of component failures, engineers often apply safety factors during component design in order to ensure that the design service life will exceed the expected time to failure [2]. Reliability of a system is generally a function of design and relies heavily on theoretical analysis [1] along with testing to verify safety and durability of the system and its components [2]. Given the complexity of material behaviours and the assumptions reflected in many engineering estimates of strength and life, there is potential that a prolonged service life will uncover additional problems that need to be addressed [2]. Inspection is one approach used to identify these additional problems at early stages in an effort to prevent the occurrence of failures. Such inspections can be destructive or non-destructive in nature. However, non-destructive testing (NDT) offers several benefits over destructive testing such as improved cost-effectiveness, reduction in unscheduled maintenance requirements and increased scheduled maintenance intervals [3].

Due to the large number of benefits, the aerospace industry has implemented NDT as both a method of quality control during manufacturing to identify defects, abnormalities or imperfections, and in-service to find any damage, degradation or deterioration of critical aircraft components [4]. The conventional NDT techniques employed for the inspection of aircraft materials, components and structures are liquid penetrant, magnetic particle, eddy current, ultrasonics and radiography [5]. Each NDT method has different capabilities and limitations and as such the choice of inspection technique is dependent on many factors including inspection requirements, access to the test site, ease of test method application and inspection costs [4]. For any given NDT method, there are many parameters which can potentially influence the outcome of an inspection. These are known as influential parameters [6]. Influential parameters that may affect an inspection outcome in such a way that the inspection can no longer meet its defined

objectives are defined as essential parameters [6]. These essential parameters must be considered when evaluating the capabilities of any NDT system.

During a typical flight, aircraft are subject to cyclic loading as a result of the ground-air-ground cycle (g.a.g.) [7]. These repeated loads result in cyclic stresses that can lead to microscopic physical damage to the aircraft structure and material. Even at stresses that are well below the material's ultimate strength, this damage can accumulate under continued cyclic loading until it develops into a crack that leads to failure. This damage and failure caused by cyclic loading is known as fatigue [2]. The CP-140 Aurora and CC-130 Hercules aircraft currently operated by the Royal Canadian Air Force (RCAF) are susceptible to cyclic fatigue cracks around ferrous fasteners in the bolt holes of multi-layer aluminum wing lap-joints. A schematic for a typical lap-joint cross-section is shown in Figure 1. If left unattended, these cracks can grow allowing them to reach a critical crack length that would result in material fracture [8]. Therefore, the ability to detect and monitor crack growth in these regions is critical for sustainment of safe flight operation.

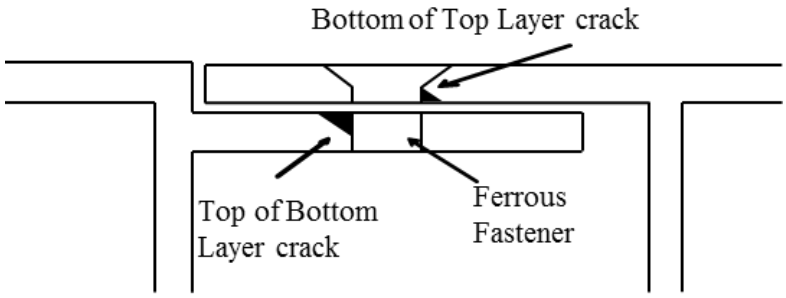

Figure 1: Cross-section of a typical lap-joint configuration showing bottom-of-top layer and top-of-bottom layer cracks along with the ferrous fastener location [8].

The current method of second layer crack detection uses bolt hole eddy current (BHEC), which requires fastener removal [9]. This fastener removal process can be quite labour intensive and there is an added risk of damage to components during disassembly [8]. Fastener removal requires the steel fastener to be manually drilled out and thus slipping of the drill bit can cause significant damage to the surrounding aluminum surface. An example of typical drill bit damage incurred during disassembly is shown in Figure 2. The minimum detectable flaw size, or $a_{90/95}$ is defined as the defect size that a NDT technique is able to reliably detect 90% of the

discontinuities of that size, 95% of the time [10]. For the current BHEC technique used on the CP-140 Aurora the $a_{90/95}$ is 0.79 mm (0.031") for electric discharge machined (EDM) notches and 0.91 mm (0.036") for fatigue cracks [9]. Pulsed eddy current (PEC) is one technique that is currently being examined as an alternative method for detecting cyclic fatigue cracks in multi-layered wing structure without fastener removal. The PEC inspection technique is employed while the ferrous fasteners are present and the fastener is used as a conduit for the magnetic flux created by the driving coil. This allows for a deeper penetration of eddy currents, while sensing coils placed on the aluminum surface pick up resultant transient responses [8]. The $a_{90/95}$ for PEC detection of second layer notches is currently unknown and existing analysis techniques require knowledge of signals obtained from defect free (blank) fastener locations in order to produce crack detection results.

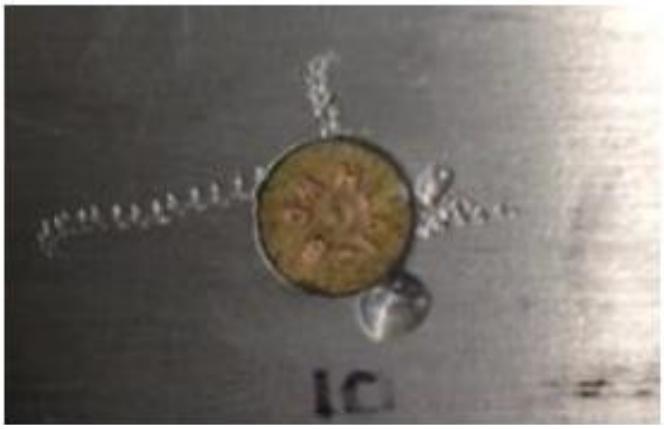

Figure 2: Typical drill bit damage incurred during removal of a steel ferrous fastener securing an aluminum lap-joint [11].

1.2 Eddy Current Testing

Eddy currents are electrical currents induced in a conductor by a time-varying magnetic field [5]. These currents flow in a circular pattern in a path orientated perpendicular to the direction of the magnetic field direction. Figure 3 shows the flow of eddy currents for two typical test piece geometries. Eddy current testing (ET) is an electromagnetic NDT method used to detect discontinuities in electrically conductive structures. The technique uses a probe with electromagnetic coils to produce an alternating magnetic field, which induces eddy currents in the conductive structure due to Faraday's Law. The magnitude and distribution of these eddy

currents vary in response to specimen properties such as electrical conductivity, magnetic permeability, geometry and discontinuities [5]. When eddy currents encounter an obstacle such as a crack, the normal path and strength of the currents are disrupted and changes due to this disruption can be observed using an impedance plane display.

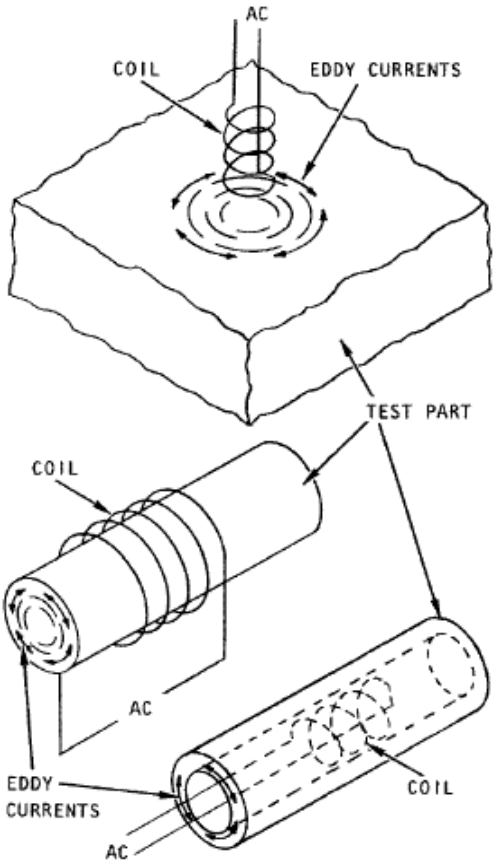

Figure 3: Flow of eddy currents in typical test piece geometries indicating that eddy currents flow in a circular pattern perpendicular to the applied magnetic field [5].

ET is used for a variety of applications such as detecting surface and subsurface cracks, detecting discontinuities in materials, determining material properties such as resistivity, and measuring the thickness of thin metals and coatings. However, this inspection technique is limited to electrically conductive non-ferromagnetic materials, since ferromagnetic materials may have permeability variations that can be falsely identified as flaws [5]. In ferromagnetic materials, the high relative magnetic permeability also acts as a shield against the penetration of eddy currents, and consequently the effective depth of inspection for this technique is reduced in ferromagnetic

materials [5]. For this reason, eddy current testing of ferromagnetic components is typically limited to testing for flaws that exist at or near the surface of the part.

One of the leading challenges faced when inspecting second layer wing structures in the presence of ferrous fasteners is that the magnetization of the ferromagnetic fastener overwhelms the pick-up coil response. This in turn makes it difficult to detect smaller flaws in the surrounding aluminum structure. However, greater depth of penetration can be achieved in the presence of ferromagnetic fasteners through the application of PEC [12]. Instead of the sinusoidal excitation applied in conventional ET, PEC employs a square pulse excitation whose composition can be viewed as a spectrum of discrete frequencies. It has been suggested, that based on simple skin depth relationships, PEC should be able to penetrate deeper than conventional ET [13].

1.3 Outlier Detection

The concept of outlier detection encompasses a broad spectrum of techniques [14]. For the purpose of this work, an outlier is defined as an observation that appears to be inconsistent with the remainder of a data set [15]. Outlier detection is considered to be a critical task in many safety critical environments because outliers are an indication of abnormal conditions. The three fundamental types of outlier detection are as follows [14]:

- Type 1 (unsupervised clustering) – Outliers are determined with no prior knowledge of the data set.
- Type 2 (supervised classification) – This approach requires prior knowledge of both normal and abnormal data. Here, both the normal and abnormal classes are taught and the algorithm learns to sort new data into the pre-defined groups.
- Type 3 (semi-supervised recognition) – This approach only requires prior knowledge of data classified as normal. Here, the normal class is taught and the algorithm learns to recognize abnormality.

Many Type 1 approaches seek to identify outliers first, while fitting a system model to the remaining data until no more outliers are detected. Alternatively, accommodation is a methodology that incorporates outliers into the distribution model and then employs a robust classification method [14]. These robust approaches, such as the smallest half volume (SHV)

method [16], can withstand outliers in the data and generally establish a boundary around the majority of the data, which is therefore most representative of normal behaviour [14]. Alternatively, non-robust classifier methods produce representations that are skewed when outliers are left present [14].

Type 2 classifiers such as support vector machine (SVM) and artificial neural networks are best suited to static data as the classification needs to be rebuilt from first principles if the data distribution shifts [14]. These classification methods require a good spread of both normal and abnormal data such that the data covers the entire distribution in order to allow for generalization by the chosen classification method. If any region of the distribution has not been previously seen, then this region may be classified incorrectly as there is not enough information known to accurately categorize that portion of the data [14].

If the normal condition is known, a Type 3 system such as a cluster analysis [17] can be employed to classify a new data point as normal, if it lies within a predefined boundary, or to classify the data point as an outlier if it lies outside. This type of outlier detection requires the availability of a full assortment of normal data points for training in order to permit generalization. This approach is extremely advantageous in fields where it is difficult or costly to obtain abnormal data [14] as is the case with aircraft lap-joint structures.

It is important to select an algorithm that can accurately model the data distribution and accurately highlight outlying points for a clustering classification or recognition type technique. A suitable threshold for an outlier must also be selected in order to accurately define the boundaries of normality [14].

This thesis work utilizes the basic PEC probe design investigated by Whalen [12] for multi-layer inspection in the presence of ferrous fasteners. This probe design has been further enhanced for cyclic fatigue crack detection in second layer aluminum structures through the implementation of eight differentially paired pick-up coils [11]. The statistical analysis approach described by Horan *et al*. [18], known as modified principal components analysis (MPCA), is employed to reduce PEC signals to a series of scores and eigenvectors that express as much of the data variation as possible. The MPCA is followed by both a Mahalanobis distance (MD) analysis (Type 3) [17] and a smallest half volume (SHV) analysis (Type 1) [16]. These approaches are

used to further distinguish between signals obtained in the presence of electric discharge machined (EDM) notches and those obtained from blank fastener locations [11] [19].

1.4 Objective

The goal of this work is to evaluate and further enhance the equipment and analysis techniques used for PEC inspection of aircraft lap-joint structures in the presence of ferrous fasteners. The inspection methods currently employed present significant limitations, as BHEC requires fastener removal and previous work done with PEC requires knowledge of blank fastener signals. Therefore, these enhancements are essential in order to maximize the detectability of second layer notches in the presence of ferrous fasteners across multiple samples without prior knowledge of unflawed behaviour in the data set. Detection without prior knowledge of unflawed behaviour is the most desirable approach due to the high cost associated with producing multiple representative calibration pieces. Also, there are a small number of flawed fastener locations currently identified in aircraft wing structures relative to the number of unflawed fastener locations. This small number of flawed fastener locations is ideal for identification of outliers using robust approaches as the majority of the data collected will exhibit normal unflawed behaviour. The result of this work has implications for the overall detection performance of this PEC system and provides critical insights regarding the challenges that may be faced when essential parameters are not accounted for prior to conducting a probability of detection (POD) study for this technique and during field deployment of the system.

1.5 Thesis Scope and Methodology

The following presents an outline of the remaining sections and methodology for this thesis.

Section 2 presents the electromagnetic theory that governs eddy current inspection. The presentation of this theory includes discussion of Maxwell's Equations, electromagnetic diffusion, skin depth effects, eddy current generation in a conductive medium and equivalent circuit models. This is followed by a description of the statistical theory pertaining to MPCA. Next, the MD cluster analysis technique is presented as a Type 3 outlier detection method for the detection of second layer defects. Finally, the theory surrounding the SHV robust statistics analysis method is outlined as an alternative defect detection approach.

Section 3 presents a literature review of PEC applications as related to inspection of second layer aircraft lap-joint structures. First, analytical works that form the foundation for transient diffusion of a magnetic field into a surrounding material are reviewed. Next, articles related to analysis of PEC signals using statistical techniques such as support vector machine (SVM), principle components analysis (PCA), independent components analysis (ICA), MPCA and MD analysis are summarized. Finally, an article detailing the derivation and application of the SHV robust statistics algorithm is examined.

Section 4 describes the experimental setup used for data collection during this thesis work. First, a series of coil based probe designs are presented along with the physical characteristics that make each of the probe designs unique. This is followed by a brief description of the data acquisition (DAQ) system design used to control system parameters such as the driving coil pulse and digitization of the pick-up coil response. Next, the physical characteristics of multiple samples are described in full detail. The details described include general dimensions and material properties along with notch lengths, orientations and locations. Slight differences in essential parameters observed between different samples are also briefly outlined. Finally, a description of the probe alignment process is presented.

Section 5 presents the signal analysis process. A typical PEC signal response is described along with justification for the portion of the signal chosen for analysis. This is followed by an overview of how the cluster analysis method is applied as a method of outlier detection. This approach is a Type 3 outlier classification methodology and, as such, information about the expected normal data (blank fastener signal response) must be known for effective classification. Previous work has relied heavily on this cluster based classification methodology. Next, improvements to the data acquisition system and post-processing analysis techniques are detailed, implemented and evaluated. A new data acquisition circuit board using an operational amplifier (op-amp) based amplification circuit is presented. This improved circuit results in a cleaner signal reproduction. Through the analysis of multiple samples, potential issues related to environmental factors, probe off-centering and edge effects become apparent. To address these issues, the cluster based classification methodology is further enhanced through mathematical manipulation of the measurement data. Finally, application of the SHV algorithm is presented as an alternative method of identifying cyclic fatigue cracks in second layer wing structures. The SHV robust statistics approach is a Type 1 outlier classification methodology, which means that

the method is capable of blind outlier detection. Given that appropriate calibration samples are not easily generated, it may not be practical to obtain advanced knowledge about blank fastener signals prior to an on-aircraft inspection. Therefore, this blind detection approach is highly desirable for field deployment of this PEC system.

Section 6 presents the experimental results obtained. Measurements were taken from seven multi-fastener test pieces representative of the structure of a CP-140 Aurora (Lockheed P-3 Orion). Four different PEC probe configurations are evaluated and the effect of probe driving coil core diameter along with differential pick-up coil pair spacing are examined. This is followed by an overview of results obtained for multiple single sample detection cases (samples evaluated against their own blank fastener signals only) and one combined sample detection case (samples evaluated by combining blank fastener signals obtained from multiple samples). Previous work [8] has only examined detection for the single sample case with a limited number of samples. In this section, multiple samples are examined and an attempt is made to combine data collected from multiple samples for collective analysis. Next, a series of simulated detection results based on both the cluster analysis and SHV analysis approaches are presented. The blank fastener data used in these simulations is randomly generated in order to create a realistic statistical data spread from a limited number of real blank fastener sites. Data obtained from fasteners with EDM notches is used to represent signals obtained from fastener sites containing cyclic fatigue cracks.

Section 7 discusses the significance of results obtained from evaluation of four different PEC probe configurations and provides a justification for why a particular probe was selected. Next, the selection of an appropriate analysis technique is discussed. This is done by comparing the results obtained before and after the application of analysis enhancements, specifically developed to deal with essential parameters such as environmental factors, probe off-centering and fastener proximity to the lap-joint edge. Simulation results for both the Type 3 (MD) and Type 1 (SHV) outlier detection methodologies are also compared. Advantages of using the SHV outlier detection methodology for practical inspection application are outlined along with some of the disadvantages of using other popular outlier detection methodologies. This is followed by a brief discussion of the consequence of increasing false call rates to improve defect detectability along with a description of some challenges faced when trying to determine a minimum detectable flaw size.

Section 8 summarises the results of this work including the implications that these findings have on further development of this PEC system for the inspection of aircraft lap-joint structures. Recommendations for future work required to make this technique deployable for aircraft second layer crack detection are also outlined.

2. Theory

2.1 General

The purpose of this Section is to provide an overview of conventional eddy current and pulsed eddy current (PEC) inspection theories through the development of the physical principles that govern these inspection techniques. Maxwell's Equations are presented followed by an explanation of how electromagnetic fields diffuse in conducting material. Next, an explanation of eddy current generation is presented followed by a series of basic circuit model solutions for different transient system configurations. The theory surrounding modified principal components analysis (MPCA) is presented, followed by an explanation of how the scores generated from the MPCA can be used to determine the Mahalanobis distance (MD) which is compared to a decision threshold. Next, the robust statistics approach known as smallest half volume (SHV) is outlined as a potential automated detection method. Finally, the theory used to randomly generate covariance matrices is presented as a method of statistically expanding a real measured data set.

2.2 Maxwell's Equations

In order to gain a better appreciation for the physical principals that govern the PEC technique, the four general Maxwell's Equations are listed [20]:

$$\nabla \cdot \mathbf{E} = \frac{\rho}{\epsilon_o} \tag{2.1}$$

(Gauss' Law)

$$\nabla \cdot \mathbf{B} = 0 \tag{2.2}$$

(No Monopoles)

$$\nabla \times \mathbf{E} = -\frac{\partial \mathbf{B}}{\partial t} \tag{2.3}$$

(Faraday's Law)

$$\nabla \times \mathbf{B} = \mu_o \mathbf{J} + \mu_o \epsilon_o \frac{\partial \mathbf{E}}{\partial t} \tag{2.4}$$

(Ampère's Law with Maxwell's Correction)

where **E** is the electric field, **B** is the magnetic field, **J** is the current density, ρ is the charge density, ϵ_o is the permittivity of free space and μ_o is the permeability of free space.

For a linear and homogeneous medium the following relationships are valid [20]:

$$\mathbf{H} = {}^{1}\!/_{\mu}\,\mathbf{B} \tag{2.5}$$

$$\mathbf{D} = \epsilon \mathbf{E} \tag{2.6}$$

$$\mathbf{J}_f = \sigma \mathbf{E} \tag{2.7}$$

where **H** is the magnetic field intensity that is related to the magnetic field as a function of the permeability, μ. The electric displacement, **D** is related to the electric field **E** as a function of the permittivity, ϵ. Equation 2.7 is known as Ohm's Law. This equation is applicable in good conductors and describes how the free current density, $\mathbf{J}_f$, is proportional to the electric field, **E**, as a function of the materials conductivity, σ. In Equation 2.8, ρ_f is the free charge density or free charge-per-unit volume. From Ohm's law, Maxwell's Equations in the presence of a linear media can be rewritten as follows [20]:

$$\nabla \cdot \mathbf{E} = \frac{\rho_f}{\epsilon} \tag{2.8}$$

$$\nabla \times \mathbf{E} = -\frac{\partial \mathbf{B}}{\partial t} \tag{2.9}$$

$$\nabla \cdot \mathbf{B} = 0 \tag{2.10}$$

$$\nabla \times \mathbf{B} = \mu\sigma \mathbf{E} + \mu\epsilon \frac{\partial \mathbf{E}}{\partial t} \tag{2.11}$$

2.3 Electromagnetic Diffusion Equations

With Maxwell's Equations for matter defined, the equations that define how magnetic fields flow in a conductor will now be derived. First, taking Equation 2.9 and applying the curl operator, the following equation is obtained:

$$\boldsymbol{\nabla} \times (\boldsymbol{\nabla} \times \mathbf{E}) = -\nabla \times \frac{\partial \mathbf{B}}{\partial t} \tag{2.12}$$

Equation 2.12 can be rearranged by applying the following vector identity [20]:

$$\boldsymbol{\nabla} \times (\boldsymbol{\nabla} \times \mathbf{A}) = \boldsymbol{\nabla}(\boldsymbol{\nabla} \cdot \mathbf{A}) - \nabla^2 \mathbf{A} \tag{2.13}$$

where **A** is an arbitrary vector. This rearrangement, combined with commutation of the position and time derivatives, results in the following equation:

$$\boldsymbol{\nabla}(\boldsymbol{\nabla} \cdot \mathbf{E}) - \nabla^2 \mathbf{E} = -\frac{\partial}{\partial t}(\boldsymbol{\nabla} \times \mathbf{B}) \tag{2.14}$$

For a good conductor it can be shown that any free surface charge will dissipate extremely fast and therefore, $\rho_f = 0$ [20]. In this case, Equation 2.8 reduces to $\boldsymbol{\nabla} \cdot \mathbf{E} = 0$. Using this result, Equation 2.14 can be rewritten as follows:

$$\nabla^2 \mathbf{E} = \frac{\partial}{\partial t}(\boldsymbol{\nabla} \times \mathbf{B}) \tag{2.15}$$

Substituting Equation 2.11 yields:

$$\nabla^2 \mathbf{E} = \frac{\partial}{\partial t}\left(\mu\sigma \mathbf{E} + \mu\epsilon \frac{\partial \mathbf{E}}{\partial t}\right) \tag{2.16}$$

Equation 2.16 can be rearranged as follows:

$$\boldsymbol{\nabla}^2 \mathbf{E} = \mu\sigma \frac{\partial \mathbf{E}}{\partial t} + \mu\epsilon \frac{\partial^2 \mathbf{E}}{\partial t^2} \tag{2.17}$$

This equation is now in the form of Maxwell's modified wave equation [20]. Similarly, an expression can be obtained for the magnetic field **B** such that it is decoupled from the electric field. This action yields the following result [20]:

$$\nabla^2 \mathbf{B} = \mu\sigma \frac{\partial \mathbf{B}}{\partial t} + \mu\epsilon \frac{\partial^2 \mathbf{B}}{\partial t^2} \tag{2.18}$$

2.4 Skin Depth Theory

Material thickness and depth of penetration must also be taken into consideration as eddy current density and flux attenuates exponentially with depth [13]. Additionally, test results will be affected when the depth of penetration exceeds the material thickness. The standard depth of penetration is defined as follows [3]:

$$d = 50\left(\frac{\rho}{f\mu_r}\right)^{\frac{1}{2}} mm \quad or \quad d = 2\left(\frac{\rho}{f\mu_r}\right)^{\frac{1}{2}} in \tag{2.19}$$

where ρ is the electrical resistivity in $\mu\Omega$-cm, f is the excitation frequency in Hz and μ_r is the dimensionless relative permeability.

2.5 Eddy Current Generation

The generation of eddy currents in conductive materials is based on Faraday's Law, which describes how a changing magnetic field induces an electric field or electromotive force (emf). The emf $\mathcal{E}$ can be expressed in the form of Faraday's law of induction, which states that the induced emf in a closed loop equals the negative of the time rate of change of magnetic flux, Φ, through the loop [21]. This can be obtained by applying the curl theorem to Equation 2.3:

$$\mathcal{E} = -\oint \boldsymbol{E} \cdot d\boldsymbol{l} = -\int \frac{\partial \mathbf{B}}{\partial t} \cdot d\mathbf{a} = -\frac{d\Phi}{dt} \tag{2.20}$$

The magnetic flux is related to the magnetic field by the area integral $\Phi = \int \mathbf{B} \cdot d\mathbf{a}$ where $d\mathbf{a}$ is the area enclosed by the loop. The minus sign in the equation is Lenz's Law, which states that the direction of any magnetic induction effect is such as to oppose the cause of the effect [21]. In conductive materials, the emf drives eddy currents, which oppose this change in magnetic flux. For a uniform field, as shown by the curl theorem treatment of Equation 2.3 as expressed by Equation 2.20, these eddy currents are constrained to flow in closed loops within the inspected

material, and thus generate their own magnetic fields. These fields in combination with the fields that excite the currents can be detected by sensors such as electromagnetic induction in a coil or a system of coils [3].

2.6 Equivalent Circuit Models

In PEC, a step function (square wave pulse) is used to apply a voltage to an excitation coil. During the near instantaneous application of this voltage, the current through the excitation coil exponentially approaches a constant, which is a function of the resistance in the circuit and inductance of the coil. In the absence of a pick-up coil, the simple R-L circuit shown in Figure 4 can be used to determine the response of the excitation coil.

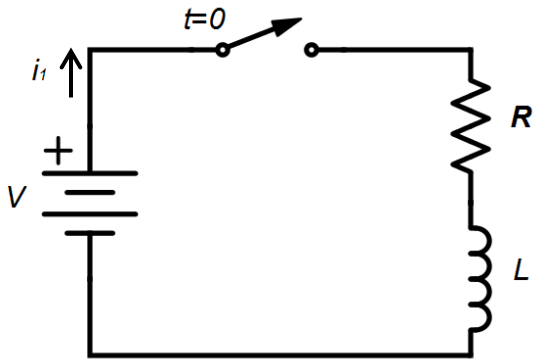

Figure 4: RL circuit representing a typical PEC excitation coil [22].

The circuit can be solved using Kirchhoff's loop rule, which states that the algebraic sum of the potential differences in any loop, including those associated with emfs and those of resistive elements must equal zero [21]:

$$\sum V = 0 \tag{2.21}$$

Applying this law to the equivalent circuit in Figure 4 results in the following equation [22]:

$$V - i(t)R - L\frac{di(t)}{dt} = 0 \tag{2.22}$$

After the switch is closed, the current will build until a steady state value is reached. Applying the boundary condition that $V = 0$ at $t = 0$, the following solution can be obtained [20]:

$$i(t) = \frac{V}{R}\left(1 - e^{-\frac{R}{L}t}\right) \tag{2.23}$$

The steady-state response of the system as shown in Figure 5 can be determined by taking the limit as t approaches infinity.

$$\lim_{t\to\infty} i(t) = \frac{V}{R}\left(1 - e^{-\frac{t}{\tau_c}}\right) = \frac{V}{R} \tag{2.24}$$

where the relaxation time is:

$$\tau_c = \frac{L}{R} \tag{2.25}$$

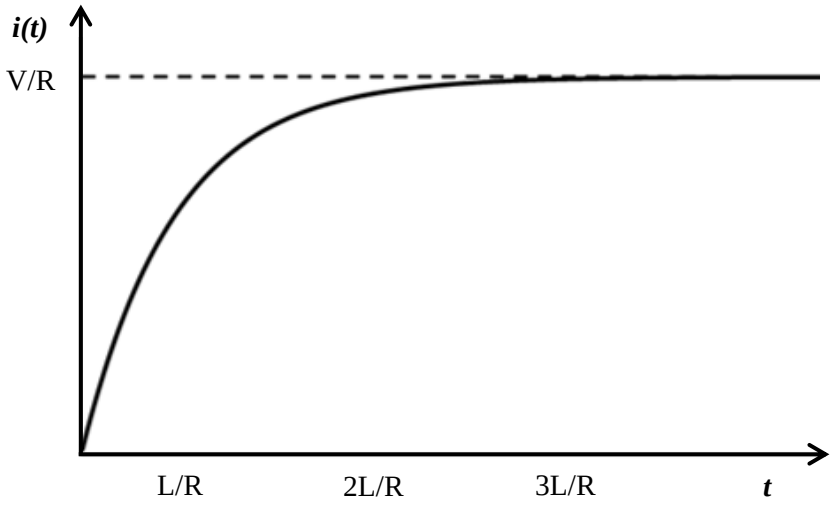

Figure 5: Plot of the resulting transient current produced when the switch is instantaneously closed for the circuit diagram shown in Figure 4 as represented by Equation 2.23 [20].

To more accurately model PEC testing, a second loop must be added to represent the pick-up coil response to the emf generated by the driving coil. The new equivalent circuit is shown in Figure 6 with all related variables defined in Table 1.

Table 1: Description of variables for the circuit diagram shown in Figure 6.

Variable	Description
L_1	Driving coil self-inductance
R_1	Driving coil resistance
i_1	Current through driving coil
M_{12}	Mutual inductance
L_2	Pick-up coil inductance
R_2	Pick-up coil resistance
i_2	Current in pick-up coil
V	Input Voltage

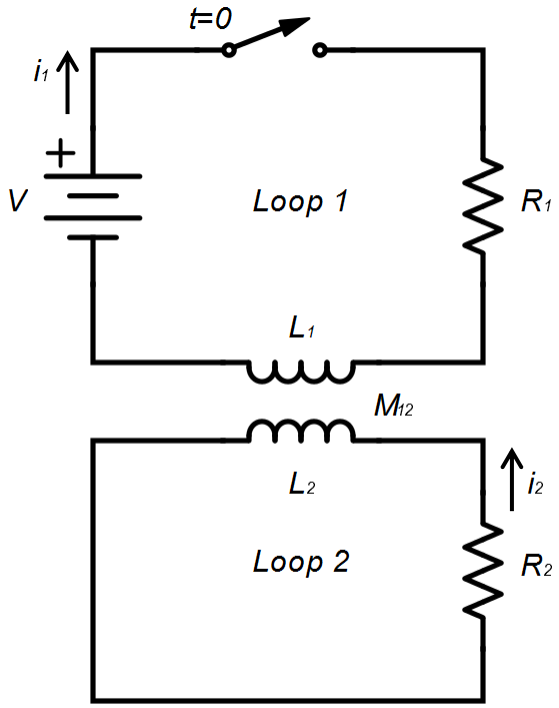

Figure 6: Equivalent circuit diagram for a PEC driving coil coupled with a single pick-up coil [23].

The close proximity of the first and second equivalent circuits results in a mutual inductance between the two elements, where the mutually induced emfs are given by the following equations [21]:

$$\mathcal{E}_1 = -M_{12}\frac{di_2}{dt} \quad and \quad \mathcal{E}_2 = -M_{21}\frac{di_1}{dt} \quad where \quad M_{12} = M_{21} \tag{2.26}$$

Thus, the application of Kirchhoff's loop rule gives rise to the following governing equations representing each closed loop of the equivalent circuit [23]:

$$L_1\frac{di_1}{dt} + R_1 i_1 = M_{12}\frac{di_2}{dt} + V_o U(t) \tag{2.27}$$

$$L_2\frac{di_2}{dt} + R_2 i_2 = M_{12}\frac{di_1}{dt} \tag{2.28}$$

where all variables are described in Table 1 and $U(t)$ is the step function. Taking the Laplace transform of Equations 2.27 and 2.28 and subsequently rearranging and solving these equations for i_2 yields the following [23]:

$$i_2(t) = \frac{M_{12}V_o(e^{-\alpha_2 t} - e^{-\alpha_1 t})}{(\alpha_1 - \alpha_2)\left(L_1L_2 - {M_{12}}^2\right)} \tag{2.29}$$

where the expression for the inverse relaxation times ${}^1/_{\tau_1} = \alpha_1,\ {}^1/_{\tau_2} = \alpha_2$ are:

$$\alpha_1, \alpha_2 = \frac{(L_1R_2 + L_2R_1) \pm \sqrt{(L_1R_2 + L_2R_1)^2 - 4R_1R_2\left(L_1L_2 - {M_{12}}^2\right)}}{2\left(L_1L_2 - {M_{12}}^2\right)} \tag{2.30}$$

A graphical representation of a typical mutual inductance response for the transient response to a step function excitation is shown in Figure 7:

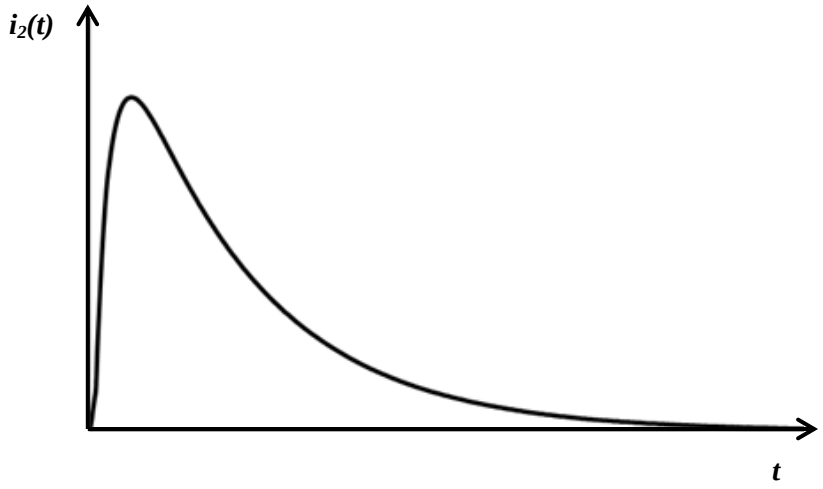

Figure 7: Typical transient current produced when the switch is instantaneously closed for the mutual inductance circuit shown in Figure 6 as represented by Equation 2.29.

The introduction of a conductive sample can be treated as a third circuit element with the addition of another mutual inductance relationship. In this case, boundary value problems incorporating Equations 2.1 to 2.4 will need to be solved in order to determine an analytical solution. This complex three-way mutual inductance relationship is depicted in Figure 8. Analytic solutions for simple rod geometries that incorporate all electromagnetic interactions have been produced by Desjardins *et al*. [24].

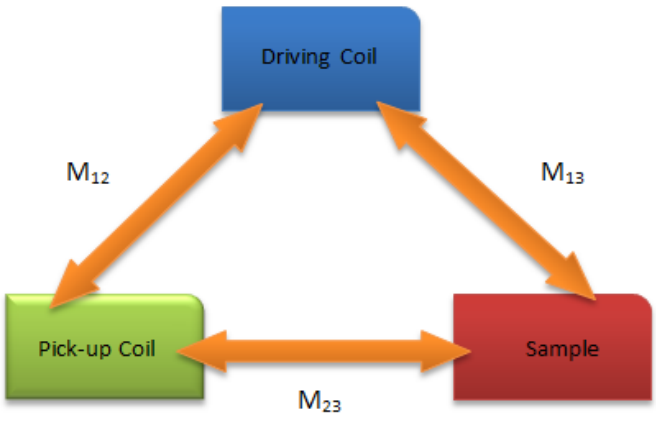

Figure 8: Graphical representation of a three-way mutual inductance relationship between a PEC driving coil, a single pick-up coil and the conductive sample being evaluated.

2.7 Modified Principal Components Analysis (MPCA)

MPCA is a least squares method used to reduce PEC signals to a series of eigenvectors and scores which best represent the maximum variance between measured signals [17] [25]. The MPCA method does not use subtraction of the average response as is the case for conventional PCA [25]. If we assume a series of *p* signal measurements $\boldsymbol{Y}_j$ with each measurement having *n* data points such that $\boldsymbol{Y}$ forms a matrix of dimension (*n* x *p)*, then a column vector **v**, that does the best job representing $\boldsymbol{Y}$ in a least squares sense is the desired solution. Thus, the column vector $\boldsymbol{Y}_j$ can be written as follows [25]:

$$\boldsymbol{Y}_j = s_j \mathbf{v} \tag{2.31}$$

where s_j is the principal component score and **v** is chosen in order to minimize the residual sum of squares, *SSR*, such that

$$SSR = \sum_{i=1}^{n}\sum_{j=1}^{p}\left(Y_{ij} - s_j \mathrm{v}_i\right)^2 = \sum_{i=1}^{n}\sum_{j=1}^{p}\left(Y_{ij}\right)^2 - 2\sum_{i=1}^{n}\sum_{j=1}^{p} Y_{ij} s_j \mathrm{v}_i + \sum_{i=1}^{n}\sum_{j=1}^{p} s_j^2 \mathrm{v}_i^2 \tag{2.32}$$

where v_i is the i[th] element of **v**. Next, it is assumed that **v** is normalized [25].

$$\sum_{i=1}^{n} \mathrm{v}_i \mathrm{v}_i = \mathbf{v}^{\mathbf{T}}\mathbf{v} = 1 \tag{2.33}$$

Thus, the coefficient s_j can be obtained as the scalar product of $\boldsymbol{Y}_j$ and **v** which results in the following expression [25]:

$$s_j = \sum_{k=1}^{n} Y_{kj} \mathrm{v}_k \tag{2.34}$$

where Y_{kj} is the k[th] element of $\boldsymbol{Y}_j$. Equation 2.34 can be expressed in matrix notation as follows:

$$\boldsymbol{s} = \boldsymbol{Y}^T \mathbf{v} \tag{2.35}$$

Using the normalized condition and Equation 2.34, it can be shown that Equation 2.32 can be reduced to the following [25]:

$$SSR = \sum_{i=1}^{n}\sum_{j=1}^{p} {Y_{ij}}^2 - \sum_{j=1}^{p} {s_j}^2 \tag{2.36}$$

In order to minimize the SSR, we must maximize the second term in Equation 2.36. Assuming normalization, the second term of Equation 2.36 can be expressed as follows [25]:

$$\sum_{j=1}^{p} {s_j}^2 = \mathbf{s^T s} = \mathbf{v^T Y Y^T v} \tag{2.37}$$

This constrained optimization problem can be solved using the method of Lagrange multipliers [17]:

$$\mathcal{L} = \mathbf{v^T Y Y^T v} - \lambda\left(\mathbf{v^T v} - 1\right) \tag{2.38}$$

where λ is the Lagrange multiplier that enforces the normalization condition of **v**. Taking the derivative of Equation 2.38 with respect to **v** yields the following:

$$\frac{d\mathcal{L}}{d\mathbf{v}} = 2\mathbf{Y Y^T v} - 2\lambda\mathbf{v} \tag{2.39}$$

Subsequently, setting this equation to zero and solving yields the standard equation for eigenvectors and eigenvalues [17]:

$$\boldsymbol{A}\mathbf{v} - \lambda\mathbf{v} = \mathbf{0}, \quad \boldsymbol{A} = \mathbf{Y Y^T} \tag{2.40}$$

This shows that an eigenvector of $\mathbf{Y Y^T}$ will do the best possible job at representing the column vectors in **Y**. Thus, the eigenvector with the largest eigenvalue will describe more of **Y** than any other vector. Similarly, the eigenvector with the second-largest eigenvalue does the best job of representing the residual left over in **Y** once the first eigenvector has been removed, thus deflating **Y** to form **Y'** [25]:

$$\mathbf{Y}' = \boldsymbol{Y} - \mathbf{v}\mathbf{s}^{\mathbf{T}} \tag{2.41}$$

A similar process can be followed for each successive eigenvector and thus the first m eigenvectors will do a better job of representing **Y** in a least squares sense than any other possible combination of m basis vectors [25]. The sum of the product of these vectors and coefficients can be used to reproduce the original data as follows [17]:

$$\boldsymbol{Y} = s_1\boldsymbol{V_1} + s_2\boldsymbol{V_2} + s_3\boldsymbol{V_3} + \cdots \tag{2.42}$$

By using a relatively small number of vectors (3-5), the original signal can be reproduced to a high level of accuracy (>99%), thus reducing the data variation to a manageable number of scores [8]. These scores can then be used to determine the MD [17].

2.8 Cluster Analysis Method

A cluster analysis can be defined as organizing objects based on their similarities where similar objects are placed together and dissimilar objects are placed apart. The MD is a cluster analysis distance which quantitatively describes the proximity of a point, y, from the centroid of a group of points, while adjusting for covariance in the data. The MD can be calculated using the following equation [17]:

$$MD = \sqrt{(\mathbf{y} - \bar{\mathbf{x}})'\boldsymbol{\Sigma}^{-1}(\mathbf{y} - \bar{\mathbf{x}})} \tag{2.43}$$

where $\boldsymbol{\Sigma}$ is the $n\,x\,n$ covariance matrix of the $n\,x\,p$ data matrix **X**, whose column vectors of length n correspond to individual measurements and $\bar{\mathbf{x}}$ is the row average of **X** that corresponds to the centroid of the measurements. In PEC analysis, the data matrix consists of the MPCA scores obtained from signals without notches (blanks). These scores can be used to compute the covariance matrix, which is then used to calculate the MD for all experimental data signals. Thus, in MPCA space, the MD can be thought of as a normalized measure of a notch's distance from the center of the cluster of blanks in standard deviations and will be distributed as a chi-

square with n degress of freedom. Once the MD is defined, it is then compared to a decision threshold in order to determine if the fastener hole has a notch present or not [8].

Figure 9 depicts MPCA scores with a sample MD for data collected using three P-3 Orion lap-joint samples. In this figure, blank fastener measurements taken from these three lap-joint samples (standards 22, 24 and 25) are shown inside of the blue ellipse. These points make up the data matrix **X**, while their average can be used to compute the centroid $\bar{\mathbf{x}}$. The MD shown by the red line is used to quantify a distance from this centroid to the point outside of the blue ellipse, which in this case represents a fastener site containing a 5.08 mm EDM notch. In Figure 9, the blue ellipse can be viewed as the threshold. Points that fall outside of this region will have a MD exceeding the threshold value and will be classified as having a defect present.

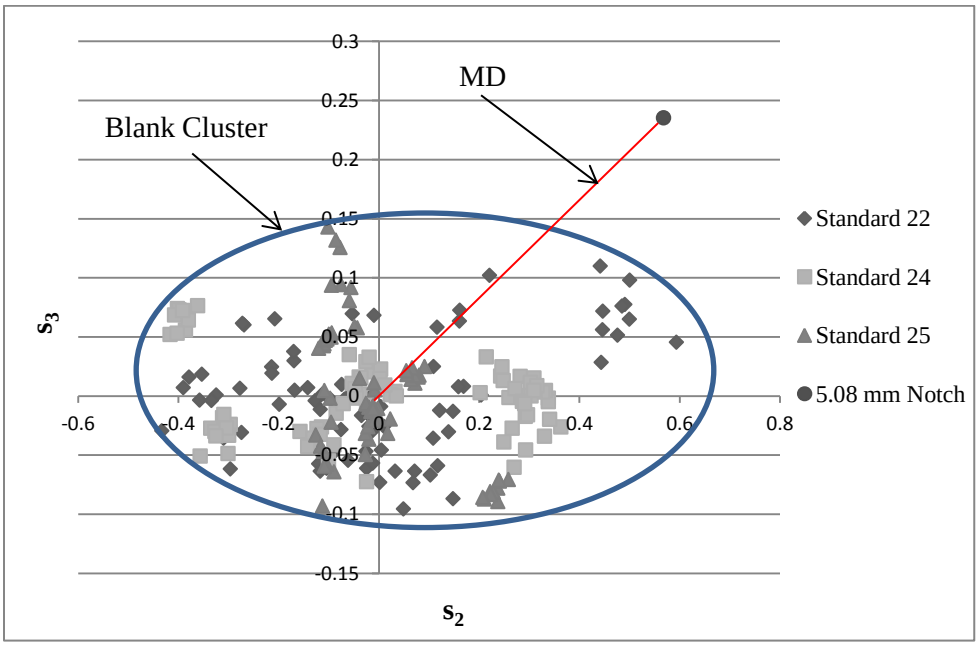

Figure 9: Plot showing blank fastener scores s_2 vs. s_3 for measurements taken from three P-3 Orion samples with blank cluster, MD and a single defect identified.

2.9 Robust Statistics Method

The calculation of the MD requires knowledge of both the data centroid, $\bar{\mathbf{x}}$, and the covariance matrix, **Σ**. Both of these are affected by the presence of outliers, especially the covariance matrix as it depends on the square of the distance of each point from the centroid. The SHV algorithm is

a robust statistical method used to obtain estimates of these two quantities [16]. It is used in a slightly modified form here in order to obtain better estimates than the original method provides. Initially, the algorithm scales the data by column (scores) by subtracting out the median value and dividing by the mean average deviation [26]. This brings all the data to approximately the same scale, similarly to using z scores in conventional statistics, but is more stable with respect to outliers. Next, the algorithm computes the length, L_{ij} between each pair of scaled data points *i* and *j* as [16]:

$$L_{ij} = \sqrt{\sum_{k=1}^{p} (x_{ik} - x_{jk})^2} \tag{2.44}$$

where the summation is over all p dimensions (scores). Once the vector lengths between observations are calculated, they are then stored in an $n\ x\ n$ distance matrix and each column is sorted in ascending order. Next, for each column the first $n/2$ smallest distances are summed. Since each column represents one of the observations, the column with the smallest sum thus represents the column with the tightest cloud of $(n/2) - 1$ observations around it. This use of a distance matrix provides a quick way of determining which group of $n/2$ observations is most internally similar [14]. Once the $n/2$ most similar observations (the points that are the most clustered together) have been selected, their covariance matrix can then be easily calculated using the unscaled data. Finally, the MD can be calculated for all n observations and subsequently used to identify outliers [16]. The modification that has been applied in this work, is the use of an arbitrary data fraction, h, ($h > n/2$) rather than $n/2$, when selecting the cluster of data points used in determining the tightest group of scaled data. This is followed by computing the mean and covariance matrix used in the MD calculation.

2.10 Randomly Generating Covariance Matrices

When the number of samples available for testing are limited, it is sometimes necessary to generate random data with the same statistical distribution as the real measured data. Given a data matrix, **S**, with rows composed of m entries which are individually random numbers with zero mean and unit variance, the $m\ x\ m$ covariance matrix, **V**, is given by the following [27]:

$$\mathbf{V} = \mathbf{S}^T\mathbf{S} \tag{2.45}$$

Thus, the expected value of $\mathbf{V}$ is the $m\,x\,m$ identity matrix. Next, a specific covariance matrix generated by real data $\acute{\mathbf{V}}$ is considered. This is a real symmetric positive semi-definite matrix and as such can be decomposed using a process known as Cholesky decomposition [28], such that

$$\acute{\mathbf{V}} = \mathbf{C}^T\mathbf{C} \tag{2.46}$$

where

$$\mathbf{C} = \begin{bmatrix} c_{1,1} & c_{1,2} & \cdots & c_{1,m-1} & c_{1,m} \\ 0 & c_{2,2} & \cdots & c_{2,m-1} & c_{2,m} \\ \vdots & \vdots & \ddots & \vdots & \vdots \\ 0 & 0 & \cdots & c_{m-1,m-1} & c_{m-1,m} \\ 0 & 0 & \cdots & 0 & c_{m,m} \end{bmatrix} \tag{2.47}$$

Next, consider the expected value of the matrix $\mathbf{W}$.

$$E(\mathbf{W}) = E(\mathbf{C}^T\mathbf{S}^T\mathbf{S}\mathbf{C}) \tag{2.48}$$

Since the C matrices are constant, then the expected value can be rewritten as follows [27]:

$$E(\mathbf{W}) = \mathbf{C}^T E(\mathbf{S}^T\mathbf{S})\mathbf{C} = \mathbf{C}^T\mathbf{C} = \acute{\mathbf{V}} \tag{2.49}$$

Consequently, the random number matrix $\acute{\mathbf{S}} = \mathbf{S}\mathbf{C}$, has the same distribution as the data used to generate the original covariance matrix, $\acute{\mathbf{V}}$, except the column mean of $\acute{\mathbf{S}}$ is 0, while the column means of the original data matrix is non-zero. A random matrix with the same distribution and means as the original data matrix can subsequently be derived by adding the column means to the values of $\acute{\boldsymbol{S}}$ [27].

3. Literature Review

3.1 General

A literature review of PEC as relevant to inspection of second layer aircraft lap-joint structures was performed. First, the fundamental analytical works that form the basis for transient diffusion of a magnetic field into a surrounding medium are summarized. Publications related to PEC analysis using statistical techniques such as support vector machine (SVM), principle components analysis (PCA), independent components analysis (ICA), modified principal components analysis (MPCA) and Mahalanobis distance were also examined. Finally, a derivation and application of the smallest half volume (SHV) robust statistics model was examined because of its Type 1 outlier detection capabilities.

3.2 Analytical Work

In 1921, Wwedensky [29] developed one of the earliest examples of the application of magnetic diffusion theory to cylindrical boundary value problems. His formulation described the time-dependent or transient diffusion of an abruptly applied uniform magnetic field into a long cylindrical conductor. Wwedensky's assumption of a uniform field implies that the field exists out to infinity, which violates Maxwell's second law $\nabla \cdot \mathbf{B} = 0$ [30]. As a consequence of this assumption, the eddy current field does not exist outside of the rod. This is problematic in eddy current applications since one seeks to measure the eddy current field in order to infer information about the conducting sample.

In 1972, Callarotti *et al*. [31] developed solutions for both conductive and non-conductive cylinders surrounded by a finite conductive shell. This formulation applies a time-dependent magnetic field oriented along the axis of the cylindrical sample. By applying the boundary conditions of continuity of tangential magnetic and electric fields across the boundary between the inner and outer regions, a solution was obtained for the relative magnetic permeability of the sample. However, only the thin-shell approximation was validated due to the increased complexity of obtaining a particular solution in the presence of a shell with significant thickness such as the aluminum structure surrounding the bore hole in an aircraft lap-joint configuration.

In 2011, Desjardins [30] developed stationary and transient solutions for the step function response of a bore hole due to a single in-hole current loop. These solutions were developed in terms of the magnetic vector potential with continuity of the magnetic vector potential maintained across the boundary of Region I (inside the bore hole) and Region II (the surrounding medium). From the solutions obtained, Desjardins concluded that the induced eddy currents will interact with the conducting volume surrounding the bore hole. Consequently, the in-hole field will diffuse into the surrounding structure inducing eddy current densities, which are expected to interact with discontinuities in the surrounding material [30].

3.3 Detecting Defects in Multi-Layer Aircraft Structures

In 2013, He *et al*. [32] investigated the use of PCA based feature extraction and SVM based automated classification as methods to categorize defects in two-layer specimens. Their paper notes that defects at different depths will affect the time-domain response of the PEC signal at different times. Thus, the shape of the response will be different for defects located at different depths. However, these amplitude changes can be weak when compared to the maximum amplitude, which may be affected by defect width. It is noted that normalisation of the signal can enlarge this weak difference which improves the ability of the PCA to extract new features from the PEC response. The principal components from the PCA can then be used as input parameters for the SVM based automated classification. When the PCA was conducted without normalization, a classification accuracy or defect detection rate of 83.4% was achieved using only the first two principal components [32]. After normalization, a classification accuracy of 100% could be achieved. Similarly, when variable lift-offs between 0 mm and 1.4 mm were introduced, the classification accuracy was 61.4% before normalization and 91.7% after [32]. In the experimental setup of He *et al.* [32], normalization prior to the PCA has been used effectively to eliminate the air gap (non-conductive layer of air between two layers of material) and lift-off effect in multi-layer structures. It is also important to note that SVM is a machine learning method of classification and as such requires the input of a training database as part of the decision-making process [32].

In the same year, Pan *et al*. [33] proposed a method of using selected frequency responses and PCA to eliminate air gap effects that hinder defect classification in two-layer structures. Their experiments were conducted using PEC with a focus on classification of surface defects,

subsurface defects and material thickness changes. One common defect found in two-layer structures is the occurrence of interlayer corrosion. In this instance, defect classification is made more difficult due to lift-off effects and interlayer air gap [33]. While previous works have considered PCA as a method of PEC defect classification, those works have only considered the time-domain response as the PCA input. The paper of Pan *et al.* [33] demonstrates the feasibility of extracting additional information by using the frequency information contained within the PEC signal as an alternative PCA input. As the excitation signal used in PEC is a square-wave signal, it is necessary to expand the Fourier series in order to obtain the periodic square wave signal in terms of fundamental frequencies and harmonic components [33]. From their work, Pan *et al*. [33] concluded that frequency responses at relatively low frequencies (3.7 to 5.4 kHz) are best for second-layer defect classification, while relatively high frequencies (12 to 25 kHz) are more suitable for locating first-layer defects. Their findings present an ability to classify both first and second layer surface and subsurface defects in the presence of air gaps varying from 0 mm to 1.4 mm by using this frequency information.

Additionally, in 2013, He *et al*. [34] compared PCA and ICA as methods of feature extraction when combined with SVM classification and prediction. In the work presented by He *et al.* [34], the analysis was first conducted by transforming the PEC signal for a multi-layer specimen from the time-domain into the frequency-domain. Features were then extracted using PCA or ICA and defect classification was performed using an SVM based algorithm. It was noted that PCA fails to process signals that are independent of each other. Alternatively, ICA is a computational method for separating a multivariable signal into additive subcomponents, which calculate independent components [34]. This method can provide better signal representation by seeking statistical independence. The results presented by He *et al.* [34] show that only 82% of defects can be classified using PCA alone. When the first two principle components are used as input for the SVM model, then this classification accuracy increases to 98.9%. When plotted graphically, the independent components are tighter clustered than the principle components, which suggests that the ICA method is more suitable for classification [34]. The ICA method, when used alone, results in a classification accuracy of 85.4%. When the ICA results are input into the SVM model this classification result increases to 100%. He *et al.* [34] concluded that ICA appears to be better than PCA for feature extraction and can be further optimized by using SVM classification. They also examined differences between time-domain responses and frequency-

domain responses and concluded that time-domain responses excel at detecting bottom layer defects, whereas frequency responses obtain better results for top layer defects [34].

3.4 Detecting Defects in the Presence of Ferrous Fasteners

In 2010, Whalen [12] demonstrated that subsurface notches initiating at the edge of a bore hole could be detected in the presence of a ferrous fastener using a PEC probe design comprised of a central driving coil combined with differentially paired pick-up coils. In Whalen's work [12], the driving coil encompasses a ferrite core and due to the core's ferromagnetic properties the flux produced by the driving coil is magnified. When this ferrite core is aligned concentrically with the head of the ferrous fastener that secures the multi-layer sample, the fastener acts as a flux conduit carrying the magnetic field to greater depths. Consequently, the resulting eddy currents that encircle the fastener are enhanced to greater depth. Whalen suggested that by increasing the ferrite core diameter relative to the ferrous fastener head diameter, more flux would be transferred to the fastener, consequently improving detection results [12].

In 2012, Desjardins *et al*. [35] concluded that PEC produces magnetization of the fastener with a consequent larger flux transfer into the surrounding structure. In this case, testing was conducted using an aluminum plate with a bore hole. Results showed that the introduction of a steel rod through the bore hole further enhances the currents induced in the vicinity of the hole and extends transient decay times [35]. This generation of larger amplitude currents results in enhanced depth of penetration of fields into the plate perpendicular to the surface. This improves the potential for defect detection as the eddy current field is disrupted in the presence of cracks projecting from the inner bore hole surface [35]. Further experiments were performed by Desjardins *et al*. [35] using a probe design that utilizes a transmit coil and two differential receive coils mounted on either side. The transmit coil was centered over a ferrous fastener placed in the bore hole of an aluminum sheet. This configuration takes advantage of the enhanced flux concentration along the ferrous fastener, which results in the same enhanced flux distribution noted above for the steel rod case. It was noted by Desjardins *et al*. [35] that this probe configuration is subject to a large signal variation as a function of rotary angle for a configuration of two cracks beneath a 1.3 mm thick aluminum plate. Overall, the results obtained by Desjardins *et al*. [35] suggest a potential to detect subsurface cracks in lap-joint structures due to the enhanced flux provided by the ferrous fastener.

In 2013, Horan *et al*. [25] presented PEC as a potential solution for inspection for stress corrosion cracking (SCC) in F/A-18 inner wing spars with thick carbon fibre-reinforced polymer (CFRP) composite wing skin. The work of Horan *et al*. [25] presented a detailed explanation of the MPCA formalism and applied it as a method of defect classification for a simulated wing spar configuration. The MPCA method differs from conventional PCA since it is does not use subtraction of the average response as with conventional PCA [17]. As with experiments conducted by Desjardins *et al*. [35], the research conducted by Horan *et al.* [25] was performed using a probe configuration consisting of a central driving coil wound around a ferrite core and two 180º opposed differentially paired pick-up coils. The simulated wing spar consisted of a 3.2 mm thick strip of 7075-T6 aluminum secured with ferrous fasteners beneath a 13 mm thick layer of Nylon 6 polymer. The simulated structure was outfitted with numerous notches of 0.2 mm width and various lengths extending from the fastener bore holes orientated in the direction of adjacent fasteners. The probe was aligned using an acrylic alignment tool. Measurements were taken from five fasteners with no cracks (blanks) and five fasteners with notches. Horan *et al*. [25] noted that the probe's transient response is sensitive to a very slight misalignment of the central driver relative to the ferrous fastener, most notably misalignment in the direction of the differential pick-up coil pair. Misalignment in the direction perpendicular to the pick-up coils produced very little effect for displacements up to 0.5 mm [25]. Using MPCA, Horan *et al.* [25] computed the first four eigenvectors to represent the acquired PEC signal and defect classification was conducted by plotting different MPCA scores against each other and looking for clustering of the data. Results obtained by Horan *et al*. [25] suggest that by plotting the third score as a function of the second, it is possible to distinguish between fastener sites with notches from those without. Horan *et al*. [25] also introduced the concept of MD as a potential real-time method for flagging extreme outliers in the data set which potentially indicates unacceptable probe misalignments.

In 2014, Babbar *et al*. [36] presented results obtained from finite element analysis (FEA) for notch detection in aircraft lap-joint structures using PEC. Transient signals were obtained by simulating a PEC probe consisting of a driving coil and eight differentially paired pick-up coils coupled with a two-layer aluminum sample containing variable crack sizes and orientations. The overall geometry of the simulated test piece was modelled to be consistent with the wing structure of a CP-140 Aurora aircraft. Babbar *et al*. [36] noted that ideally for a sample with no

defect the differential signal from each of the four pick-up coil pairs should be zero with the exception of negligible signals produced by meshing differences between the two coils that constitute a differential pair. However, in reality, the presence of a lap-joint edge on the outer surface of the top layer at 270º and the second layer edge at 90º, results in significant differential signal responses. Babbar *et al*. [36] also noted that signals were weaker and have peaks occurring at later times for second layer cracks. As with the work presented by Horan *et al*. [25], the results obtained from FEA also suggest that slight off-centering of the probe over the ferrous fastener can significantly change the amplitude and shape of the defect signal. It was observed that the signals resulting from probe off-centering in the direction of the lap-joint edge were significantly different from those obtained from the centered probe, while shifts of the probe in the direction perpendicular to the lap-joint edge appeared to be negligible [36]. As the PEC signal has information about both defects and displacement, it was noted that difficulties may arise when attempting to extract information from this type of composite signal. For this reason, the signals generated by the FEA model were analysed using PCA in order to differentiate between cracks and blanks, while accounting for variance in probe displacement [36]. The results presented by Babbar *et al*. [36] suggest that the first eigenvector is largely associated with displacement of the probe while the second eigenvector is largely related to cracks in the bottom layer. These modelling results have demonstrated the potential success of utilizing PEC in the presence of a ferrous fastener for detecting second layer cracks and determining their depths and orientations in multi-layered aluminum structures.

In 2014, Stott *et al*. [8] presented experimental results obtained from PEC measurement of a multi-layer aluminum wing skin lap-joint structure. The paper by Stott *et al*. [8] again noted the limitations of conventional ET in the presence of ferrous fasteners due to the overwhelming effect of ferrous fastener magnetization. In this case, measurements were taken using the probe design previously simulated by Babbar *et al*. [36] consisting of a central driving coil positioned concentrically inside of an array of eight differentially paired pick-up coils. The single sample evaluated consisted of a lap-joint configuration representative of a CP-140 Aurora aircraft wing structure with a series of fastener locations containing no notches and other fastener sites containing EDM notches of varying size (0.89 mm to 5.46 mm) and orientation. The data collected was analyzed using PCA with the objective of determining a quantitative measure of the distance between correlated groups represented multi-dimensionally in score space. Due to

the multiple crack sizes and orientations, discriminant analysis [17] was unsuccessful, as inserting one plane through the data in PCA space was not sufficient to separate cracks from blanks [8]. However, Stott *et al*. [8] identified that the MD could be used to calculate a relative distance between scores from a notched fastener site to those of a blank fastener site. This distance is expected to be directly correlated to crack size and the linear relationship developed between MD and crack size suggests a potential for crack sizing using PCA and MD [8]. Stott *et al*. [8] demonstrated that 97% of all notches in a single sample could be detected with 99% confidence with a 4% false call rate, while 100% of notches could be detected with 95% confidence with a 10% false call rate. Stott *et al*. [8] also noted that the consequence of a false call would be removal of the fastener at the suspect location followed by a BHEC inspection of the fastener bore hole confirming that no crack is present. Currently, fastener removal and replacement is required at all fastener locations. Hence even at an elevated false call rate, there is a potential for savings in both cost and inspection time [8].

3.5 Multivariable Outlier Detection

In 1998, Egan *et al*. [16] devised two simplified techniques for detection of multivariable outliers using robust statistics. They identified that commonly used measures such as mean and standard deviation could not appropriately deal with multiple outliers as these outliers will distort the mean. Egan *et al*. [16] also noted that the presence of these outliers would have a profound effect on the covariance matrix and thus outlying observations may be missed when analyzed using the MD. Traditional methods of outlier detection can fail without warning and thus they should be replaced by more robust methods when dealing with multivariate data [16]. Egan *et al*. [16] presented robust multivariable methods as one approach for dealing with the problems associated with the presence of multiple outliers. The two most popular robust methods, minimum volume ellipsoid (MVE) and minimum covariance determinant (MCD) were also introduced. Egan *et al*. [16] noted that these methods often require unreasonable computational efforts in higher dimensions. The two simplified methods proposed by Egan *et al*. [16] are resampling by half-means (RHM) and smallest half-volume (SHV). Both methods rely on the concept of a center for the data, rather than using the covariance matrix and only 50% of the full data set is used to develop the statistical relationship [16]. Due to their simplified nature, the RHM and SHV methods require less computation time than other robust techniques [16]. The results obtained by

Egan *et al*. [16] suggest that RHM and SHV are both superior classification methods in the presence of multiple outliers when compared to MVE and the leading technique, MCD.

4. Experimental Technique

4.1 General

The purpose of this section is to provide an overview of the experimental setup utilized for the acquisition of data as related to this work. The specifications of four distinct probe designs that differ in driving coil core diameter and differential pick-up coil pair spacing are presented. This is followed by an overview of the data acquisition (DAQ) system used to control and measure the relevant pulsed eddy current (PEC) system parameters, including the driving coil pulse and digitization of the pick-up coil responses. A circuit board design employing an operational amplifier (op-amp) based amplification circuit is introduced as a method of improving signal quality. Multiple samples representative of the wing structure of a CP-140 Aurora (Lockheed P-3 Orion) are considered. Sample physical characteristics such as material thickness, notch location, notch orientation and interlayer gap are outlined. Finally, the alignment technique used to position the probe concentrically with the fastener head is described.

4.2 Probe Enhancement

All experimental data collection was conducted using one of four different PEC probes. Each probe incorporates a central driving coil wound around a single ferrite core. Given the ferrite core's ferromagnetic properties, the magnetic flux produced by the driving coil will be magnified in the ferromagnetic fastener. This concentrates the magnetic field near the center of the probe and enhances the resulting eddy currents encircling the fastener [12]. Each probe has an array of eight pickup coils positioned symmetrically outside of the driving coil. Pick-up coils positioned 180º from each other are differentially paired, such that only the differences in their signals are collected for post-processing. The body of each probe is manufactured using a 3-D printer.

When the driving coil core is slightly larger than the ferrous fastener head, more magnetic flux can be transferred to the fastener. This results in more field lines penetrating into the fastener, thereby inducing more eddy currents in the surrounding conductive structure [12]. Three typical probe configurations used during this thesis work, Probes 1 (grey), 2 (blue) and 3 (red), are shown in Figure 10. Specification details for each probe design are presented in Table 2. The average differential pair spacing is estimated from the computer-aided design (CAD) rendering

used to create the probe body. The reduced number of turns noted in Table 2 for Probe 1 is due to a physical limitation of available space for pick-up coils and was implemented to avoid contact between adjacent pick-up coils. Probes 1 to 3 were constructed with different driving coil core diameters of 5 mm, 6 mm and 8 mm, respectively. These configurations were selected in order to investigate the effect of driving coil core diameter on the amount of flux transferred to the fastener, as postulated by Whalen [12]. Probe 4 was constructed with the same 8 mm driving coil core diameter as Probe 3. However, Probe 4 was designed to have a tighter average differential pick-up coil pair spacing than Probe 3. This was done to investigate previous FEA results, which suggest that the eddy currents concentrate near the center of the probe [12] [36].

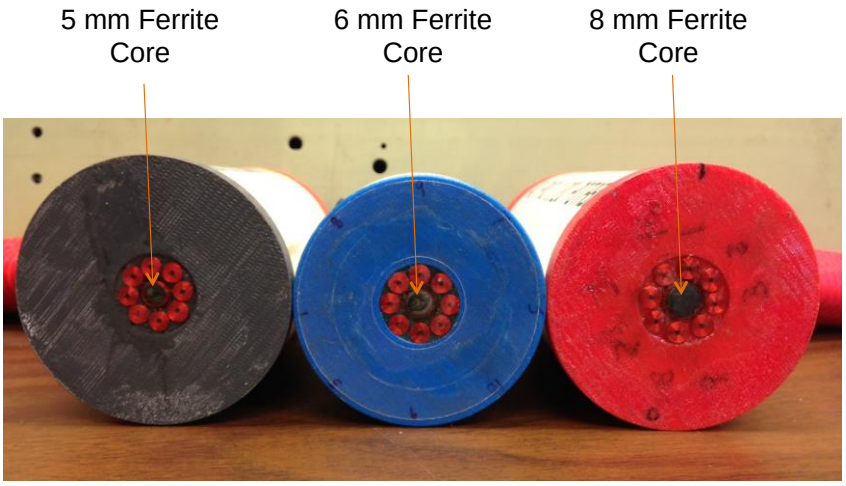

Figure 10: Three of the four probes representing varying core diameters. 5 mm (grey), 6 mm (blue) and 8 mm (red) probe configurations.

Table 2: Detailed probe specifications for the four PEC probes evaluated.

Parameter	Probe 1	Probe 2	Probe 3	Probe 4
Driving Coil Inner Diameter	5 mm	6 mm	8 mm	8 mm
Average Differential Pair Spacing	12.2 mm	13.7 mm	16.0 mm	14.7 mm
# of Turns (Pick-up Coils)	350	400	400	400
Approximate Driving Coil Resistance	21 Ω	14 Ω	18 Ω	15 Ω

4.3 Data Acquisition Equipment

When in use, the probe is connected to a custom-built amplifier circuit. A National Instruments (NI) USB-6361 data acquisition module digitizes the amplified signal at a sample rate of 100 kHz/channel and a custom software interface designed in LabVIEW 2011 is used to control acquisition parameters such as drive voltage and sample rate. A 10-volt DC pulse is used to excite the central driving coil and the differential pick-up coils sense the characteristic response of the sample due to the flux created by the driving coil. The induced response of the pick-up coils is then received through an analog input on the NI data acquisition module where it is transferred and stored on a computer for further post-processing upon measurement completion. The elements of this data acquisition process are depicted in Figure 11.

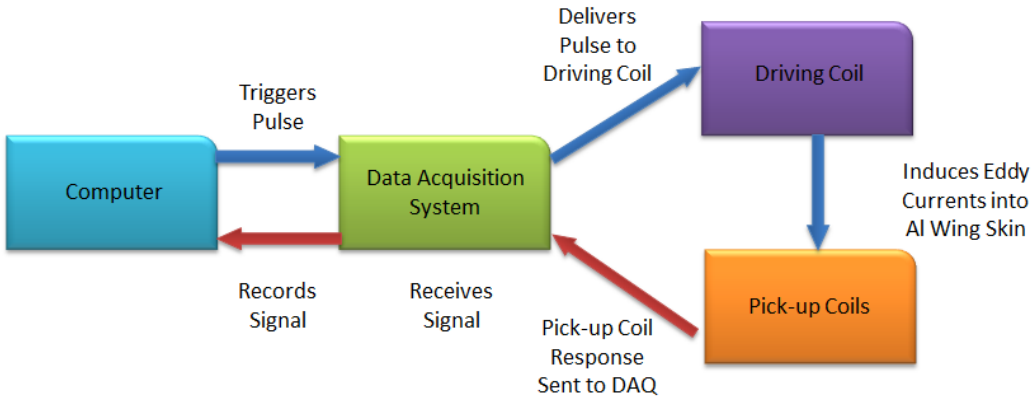

Figure 11: Flow chart depicting the flow of information in the data acquisition process.

4.4 Operational Amplifier Circuit Evaluation

Originally, the large currents required by the driving coil were obtained by using a Darlington pair in an emitter follower configuration to amplify the driver signal produced by the NI analog output. Figure 12 shows the first five eigenvectors obtained from MPCA analysis of the pick-up coil pair response signal, when the driver pulse was amplified using the Darlington pair based amplification circuit. From this figure, it can be seen that the quality of the eigenvectors starts to notably degrade after only the first three eigenvectors. In particular, the fifth eigenvector is almost exclusively noise and therefore adds little value to the signal reproduction.

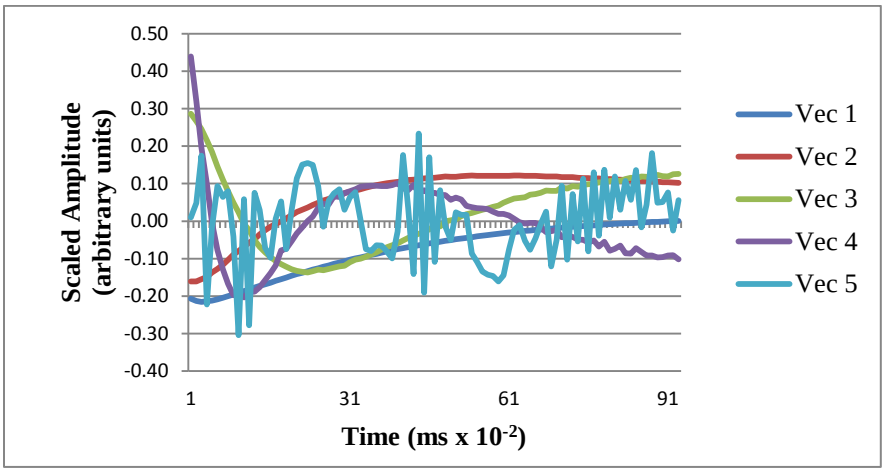

Figure 12: First five eigenvectors produced from MPCA of a pick-up coil pair response signal when the driver pulse was produced using a Darlington pair based amplification circuit.

In an effort to improve the input signal and thus the resulting signal reproduction, the transistor based amplification circuit was replaced with an operational amplifier (op-amp). An op-amp consists of a large collection of individual electronic circuits integrated on a single silicon wafer known as an integrated circuit [22]. This electronic component is based on the properties of an ideal amplifier and can be used to perform a number of operations. The op-amp used to amplify the driving coil excitation in this case was a PA75 dual power op-amp. This op-amp was wired in a noninverting configuration with the circuit diagram for this configuration shown in Figure 13.

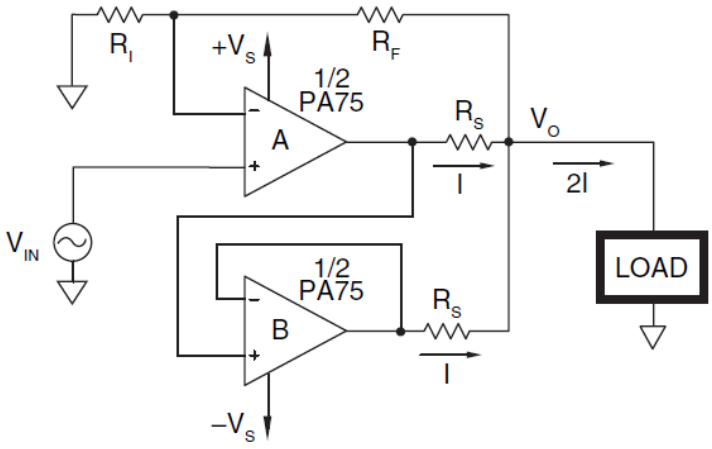

Figure 13: Circuit diagram for PA75 dual power op-amp wired in a noninverting configuration [37].

The desired closed-loop gain for the overall circuit can be achieved by setting appropriate values for two resistors, R_F and R_I, respectively, as shown in Equation 2.50 [22]. In this equation, V_{IN} is the input voltage and V_O is the desired output voltage. For the configuration used in this thesis work, these resistance values were chosen to be equal in order to achieve a closed-loop gain of two.

$$\frac{V_O}{V_{IN}} = 1 + \frac{R_F}{R_I} \tag{2.50}$$

In practical use, op-amps are not true ideal devices and thus can exhibit a number of limits in frequency response [22]. An op-amp has a finite bandwidth with an open loop gain that is a function of frequency, which results in a characteristic low pass response [22]. This characteristic low-pass filter has the potential to remove high frequency noise from the pick-up coil response signal. The PA75 op-amp used in this circuit configuration has a wide bandwidth of 1.1 MHz. The first five eigenvectors resulting from signals acquired, when the driving coil pulse is produced using this op-amp configuration, are shown in Figure 14. From this figure, it can be observed that the level of noise in the eigenvectors has been significantly reduced, particularly for the fifth eigenvector.

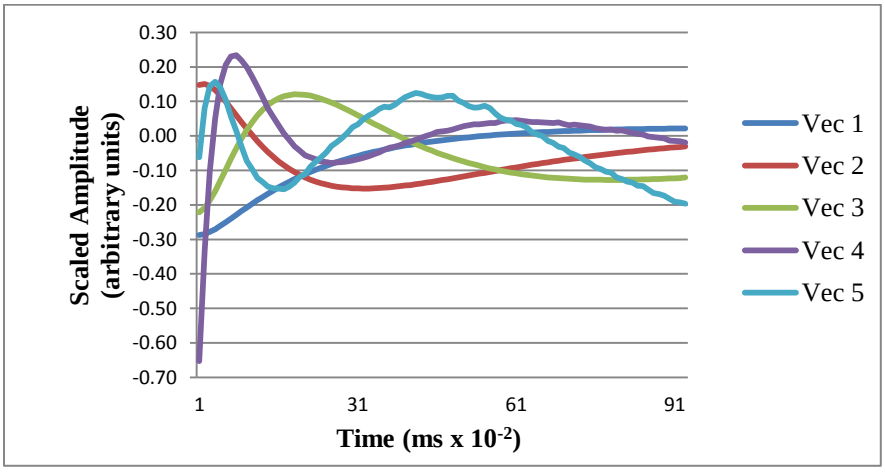

Figure 14: First five eigenvectors produced from MPCA of a pick-up coil pair response signal when the driver pulse was produced using an op-amp configured in a noninverting amplifier.

4.5 NAVAIR Sample Series Description

A series of samples were acquired for testing purposes from the Aerospace and Telecommunications Engineering Support Squadron (ATESS) located at 8 Wing Trenton. These samples were originally manufactured for the United States Naval Air Systems Command (NAVAIR) depot in Jacksonville, Florida. The samples are based on the wing lap-joint structure of the Lockheed P-3 Orion, which has the same airframe as the CP-140 Aurora used by the Royal Canadian Air Force (RCAF). These samples consist of two sections of 2024-T3 aluminum plate ranging in thickness from approximately 2.1 mm to 2.8 mm, joined together by a row of 22 to 24 ferrous fasteners in a lap-joint configuration as shown in Figure 15. Fasteners have a length of 15 mm with a head diameter of 7.0 mm and a shaft diameter of 4.5 mm [36]. The distance from each fastener to the lap-joint edge was measured using a scaled image. This fastener-to-edge distance was observed to vary by +/-1.8 mm. Additionally, the interlayer gap between the top and bottom sheets ranges between samples from 0 mm up to 0.12 mm.

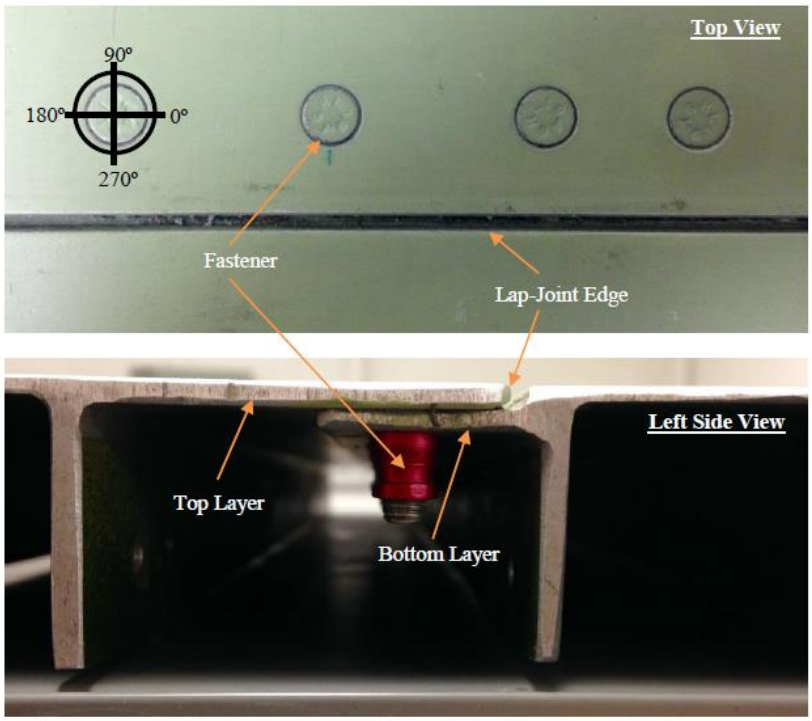

Figure 15: Top and side view of P-3 Orion sample showing the location of top and bottom layers along with fasteners and lap-joint edge.

Each sample contains blank fastener sites with no notches present in addition to a combination of bore holes containing electric discharge machined (EDM) notches at the bottom of the top layer and at the top of the bottom layer. The notches are cut at a 45° angle to the edge of the bore hole, giving a 1:1 aspect ratio and range in size from 0.76 mm (0.030") to 6.10 mm (0.240"). Characteristics of standards numbered 22-26, 28 and 32 including notch locations, notch lengths and orientations, and fastener location numbers, are noted in Table 3 to Table 9. The blank fastener locations for each sample are listed in Table 10. The thicknesses of top and bottom layers along with their interlayer gaps are presented in Table 11. The thicknesses of the top and bottom layers were obtained using ultrasonic thickness measurement [3]. With the thickness of the bottom layer known, a dial indicator was then used from the underside of each sample to measure the distance from the bottom of the top layer to the bottom of the bottom layer. The measured thickness of the bottom layer was then subtracted from the total measured value in order to quantify the interlayer gap present.

Table 3: Standard 22 notch sizes, locations and orientations.

Sample ID	Fastener #	Bottom of Top	Top of Bottom	Size mm (+/- 0.38)	Orientation CW from Lap-Joint Edge
Standard 22	1		X	3.30	135º
	2	X		1.91	270º
	3		X	1.78	225º
	4		X	0.89	90º
	5		X	5.46	45º
	6	X	X	3.30/0.89	90º/315º
	7		X	2.03	270º
	9		X	1.52	225º
	10		X	2.79	135º
	11		X	0.89	90º
	12	X	X	5.46/3.30	45º/225º
	13		X	1.52	270º
	14		X	5.08	315º
	19	X		2.79	225º
	21	X	X	0.89/2.79	45º/45º

Table 4: Standard 23 notch sizes, locations and orientations.

Sample ID	Fastener #	Bottom of Top	Top of Bottom	Size mm (+/- 0.38)	Orientation CW from Lap-Joint Edge
Standard 23	1	X	X	1.91/3.18	270º/90º
	3		X	5.33	270º
	4	X		3.18	45º
	6		X	1.65	90º
	9		X	2.16	45º
	10	X		5.33	90º
	13		X	2.79	225º
	15	X		0.89	270º
	16		X	5.08	135º
	18		X	1.52	315º
	19	X		2.54	90º
	20		X	1.27	45º
	22		X	3.18	270º
	24	X	X	1.14/2.41	315º/135º

Table 5: Standard 24 notch sizes, locations and orientations.

Sample ID	Fastener #	Bottom of Top	Top of Bottom	Size mm (+/- 0.38)	Orientation CW from Lap-Joint Edge
Standard 24	1		X	3.56	225º
	3	X	X	2.03/5.46	225º/90º
	4		X	1.14	270º
	5	X		3.43	270º
	6		X	1.52	45º
	7		X	0.89	135º
	8		X	2.16	270º
	9	X	X	5.21/Unknown	90º/225º
	11		X	2.92	90º
	12		X	2.16	270º
	13		X	5.08	45º
	15	X	X	1.27/3.43	270º
	17		X	1.65	45º
	19	X	X	2.67/2.79	270º/135º

Table 6: Standard 25 notch sizes, locations and orientations.

Sample ID	Fastener #	Bottom of Top	Top of Bottom	Size mm (+/- 0.38)	Orientation CW from Lap-Joint Edge
Standard 25	1		X	3.43	45º
	3	X	X	1.91/5.46	225º/90º
	5		X	0.76	315º
	7	X	X	3.43/1.14	90º/315º
	9		X	0.76	90º
	10	X		5.59	135º
	11		X	2.16	270º
	13		X	2.92	225º
	14		X	5.84	270º
	15	X		1.27	45º
	17		X	2.03	135º
	19		X	1.40	270º
	20	X	X	2.54/0.89	135º/270º
	21		X	3.05	90º
	22		X	2.67	225º

Table 7: Standard 26 notch sizes, locations and orientations.

Sample ID	Fastener #	Bottom of Top	Top of Bottom	Size mm (+/- 0.38)	Orientation CW from Lap-Joint Edge
Standard 26	2	X		1.65	135º
	3		X	6.10	270º
	5		X	3.18	45º
	7		X	1.27	225º
	8	X		3.30	225º
	9		X	1.02	270º
	10		X	2.16	45º
	12	X		5.46	315º
	13		X	3.05	225º
	14	X	X	0.76/5.33	270º/90º
	16		X	0.76	270º
	18	X		2.03	225º
	20	X	X	2.54/1.52	90º/225º
	21		X	3.94	315º
	22	X	X	1.27/2.79	45º/45º

Table 8: Standard 28 notch sizes, locations and orientations.

Sample ID	Fastener #	Bottom of Top	Top of Bottom	Size mm (+/- 0.38)	Orientation CW from Lap-Joint Edge
Standard 28	2		X	3.18	135º
	3		X	5.33	315º
	6		X	1.02	90º
	7		X	0.76	45º
	8	X	X	1.91/1.40	90º/270º
	9	X	X	3.40/2.16	270º/135º
	12	X		5.46	45º
	13		X	2.79	225º
	14	X	X	2.03/5.33	225º/90º
	15		X	3.30	270º
	17	X	X	1.40/1.27	135º/225º
	19	X	X	3.30/2.79	315º/135º

Table 9: Standard 32 notch sizes, locations and orientations.

Sample ID	Fastener #	Bottom of Top	Top of Bottom	Size mm (+/- 0.38)	Orientation CW from Lap-Joint Edge
Standard 32	1	X	X	1.27/3.18	90º/315º
	3		X	0.76	270º
	4	X		1.91	45º
	5		X	4.83	225º
	7		X	1.91	45º
	8	X		2.54	225º
	9		X	2.54	45º
	11		X	0.76	270º
	12		X	5.33	90º
	13	X		1.02	135º
	14	X		3.56	315º
	15		X	1.14	225º
	16		X	1.91	45º
	18		X	2.41	90º
	20		X	3.18	315º
	22	X	X	5.71/1.27	270º/225º

Table 10: P-3 Orion sample series blank fastener locations.

Sample ID	Blank Fasteners
Standard 22	8, 15, 16, 17, 18, 20, 22, 23
Standard 23	2, 5, 7, 8, 11, 12, 14, 17, 21, 23
Standard 24	2, 10, 14, 16, 18, 20, 21, 22
Standard 25	2, 4, 6, 8, 12, 16, 18
Standard 26	1, 4, 6, 11, 15, 17, 19
Standard 28	1, 4, 5, 10, 11, 16, 18, 20, 21, 22
Standard 32	2, 6, 10, 17, 19, 21, 23, 24

Table 11: P-3 Orion sample series top and bottom layer thickness with interlayer gap (uncertainties are estimated as being to within stated significant figures).

Sample ID	Top Layer Thickness (mm)	Bottom Layer Thickness (mm)	Interlayer Gap Thickness (mm)
Standard 22	2.5	2.1	0.05
Standard 23	2.6	2.1	0.12
Standard 24	2.4	2.1	0.00
Standard 25	2.5	2.1	0.03
Standard 26	2.8	2.5	0.03
Standard 28	2.5	2.2	0.06
Standard 32	2.5	2.4	0.08

4.6 Probe Alignment

During data acquisition, alignment of the probe over the fastener head is achieved using an acrylic alignment guide. The base of the guide is covered in a thin clear sheet with a center hole cut to the same size as the fastener heads. This hole is used to align the probe concentrically over the fastener head. As this is a visual alignment technique, small centering errors occur even when the inspection is performed by an experienced operator. For this reason, multiple measurements were taken at each fastener for each data set to ensure proper representation of probe placement variation within the data set. An example of the probe placement on a sample using this alignment tool is shown in Figure 16.

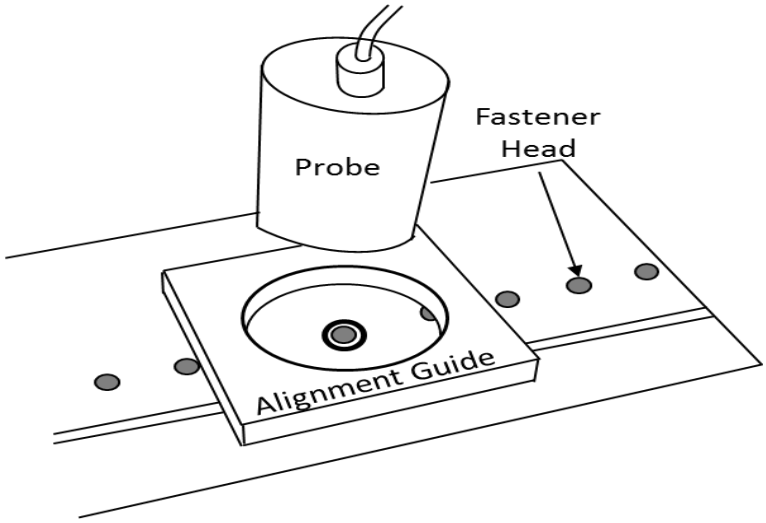

Figure 16: Probe with alignment guide and sample [8].

5. Signal Processing and Analysis

5.1 General

The purpose of this section is to provide an in-depth look at how the acquired signals are post-processed in order to determine a notch detection capability. First, the concept of signal gating is described as a method of choosing only those portions of the time-domain signal that are expected to contain the desired notch information. This ensures that the modified principle components analysis (MPCA) is only applied to the area of interest and thus other variables, whose information are contained outside of this signal gate, do not need to be considered. Next, application of the cluster analysis approach, as it applies to notch detection using the generated MPCA scores, is outlined. A methodology for removing shifts in the score space representation of the data due to environmental factors is explored. This is followed by the procedures used to eliminate variability in repeat measurements arising due to probe off-centering and to compensate for the variability in the distance between fasteners and the lap-joint edge. Finally, an overview of how robust statistics can be combined with a blank fastener simulation algorithm to achieve Type 1 (blind) outlier detection as defined in Section 1.3 is presented.

5.2 Signal Gating

All data collected was analyzed using MPCA [18] as described in Section 2.7. Given that a single DC pulse powers the driving coil, the differential pick-up coils will have a distinct response due to both magnetization, when the DC voltage is applied (front end), and demagnetization, when the DC voltage is switched off (back end). A typical signal response for a pair or differentially wired pick-up coils that are positioned 180º apart is shown in Figure 17. MPCA does not require analysis of the entire response and thus the signal for each differential pair was gated before applying the MPCA. This gating ensures that only the portion of the time domain signal that contains second layer notch information is considered. As a result, the MPCA only analyzes signal variations contained within this signal gate.

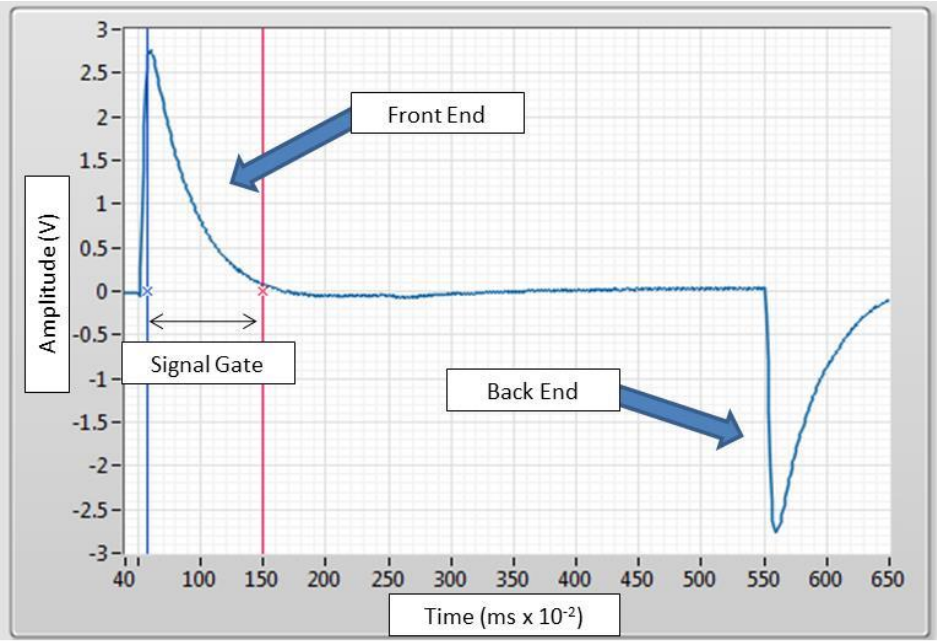

Figure 17: Raw PEC differential pick-up coil response showing the front and back end transient response along with the chosen signal gate obtained from screenshot of the LabView display.

As there is a delay between the start of the signal acquisition and the start of the pulse, there is no signal prior to 0.50 ms. As indicated by Stott [11], including the rapidly changing signal between 0.50 and 0.58 ms will cause the MPCA to focus on representation of the large variation in the signal at the beginning of the transient response. Finite Element Analysis (FEA) results have also indicated that there is no information about second layer cracks in this time window [8]. Due to rapid decay, the most useful signal would be dissipated after 1.5 ms. For this reason, signals were gated from 0.58 ms to 1.5 ms (0.92 ms signal gate) as illustrated in Figure 18. The gates were applied to each differential signal using custom built LabVIEW acquisition software. After applying the gates, eigenvectors and MPCA scores were calculated separately for each of the four differential coil pairs.

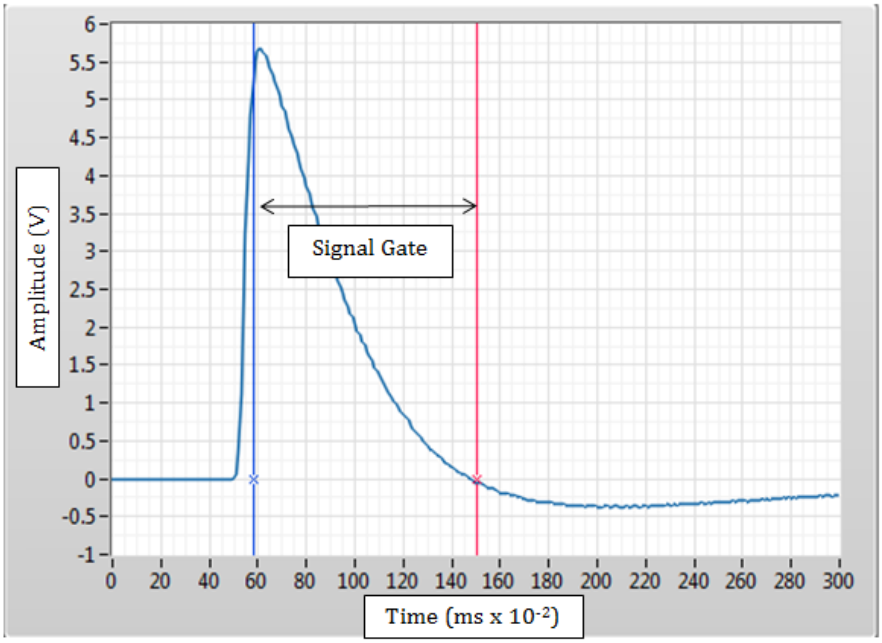

Figure 18: Raw PEC data signal showing the front end of a typical transient pick-up coil response with signal gate boundaries indicated.

5.3 Cluster Analysis

After calculating the scores, the covariance matrix was determined from the scores of known blanks for each coil pair. The MD was then calculated for each fastener, separated by coil pair and compared to a threshold value. Fasteners with a distance greater than the threshold were considered as having a notch present, while those below the threshold were considered to be blanks. In each analysis, the threshold value chosen was directly related to the desired false call rate. Detection results for each fastener, including blank fastener locations, were tabulated with the final notch detection results obtained by recording a hit if a hit was obtained on any coil pair. While this methodology results in the highest number of crack detections possible for each data set, it also increases the false call rate.

5.4 Removing Shifts Due to Environmental Factors

Given the large volume of data collection, sample measurements were acquired at different dates and times. Therefore, the data obtained was subjected to slightly different environmental conditions. Figure 19 shows a plot of s_2 vs s_4 for blank fastener scores obtained from measurement of Standard 22 (blue), Standard 24 (red) and Standard 25 (green). Here, it can be observed that differences in operating environment can result in a shift of the blank cluster from one sample to the next. The cause of this shift was isolated to environmental factors as the same shift also occurs when measurements are taken from the same sample at two different times. It is suspected that temperature could be one such environmental condition that is responsible for this shift as it has been previously demonstrated by Buck *et al.* [38] that even small variations in temperature can have a notable effect on PEC inspection results. As the ability to remove this shift is independent of cause, quantification of the effect of specific environmental factors such as temperature were not investigated in this thesis work. Fortunately, by computing the mean blank scores for a given sample data set and subtracting these means from all scores in that particular data set, this shift can be removed as illustrated in Figure 20. In this figure, it can be seen that the blank fastener scores obtained from standards 22, 24 and 25 have all been re-centered about the origin, which significantly reduces variability in the overall blank data cluster.

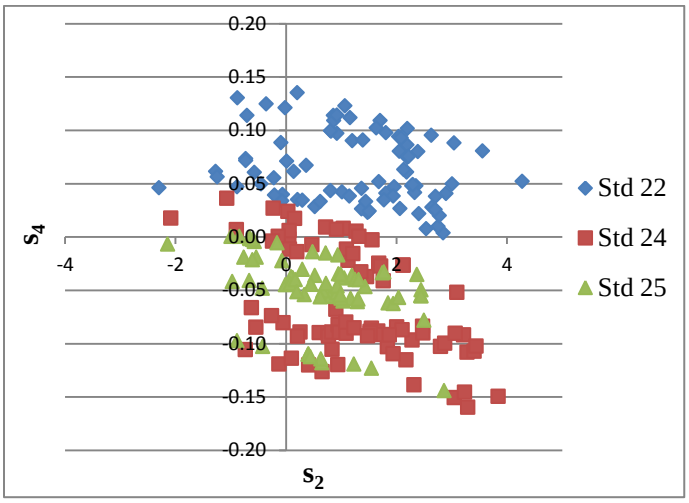

Figure 19: Plot of blank scores obtained for standards 22, 24 and 25 showing a shift in the blank clusters due to environmental factors.

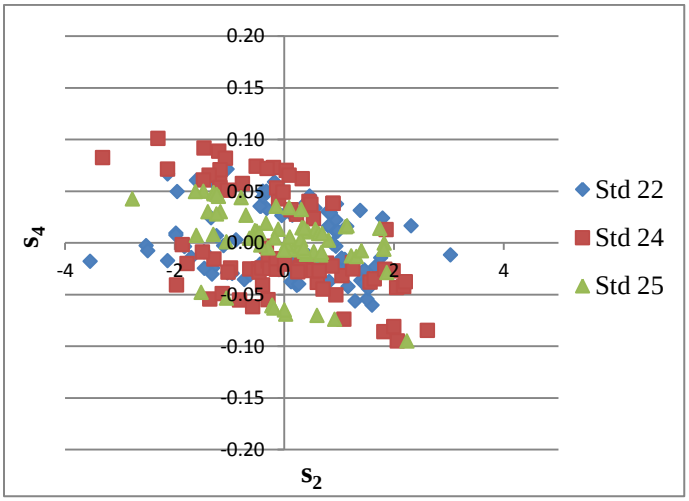

Figure 20: Plot of blank scores obtained for standards 22, 24 and 25 showing re-centered blank clusters with environmental shift removed.

5.5 Repeat Measurement Effects

Previous works by both Horan *et al.* [25] and Babbar *et al.* [36] showed that slight off-centering of the probe with respect to the ferrous fastener head can change the amplitude and shape of the resulting signal. Multiple measurements were taken at each fastener location to ensure representation of the effects of probe placement variation. The variation in repeat measurements due to horizontal off-centering (0º/180º in Figure 15) of the probe can be graphically observed by

subtracting the average of all repeat measurements for each blank fastener and plotting s_1 vs. s_2 for each sample data set. An example of the resulting relationship is shown in Figure 21. This figure shows that variation due to repeat measurements forms a linear relationship with respect to s_1 and s_2. A unitary rotation can be applied to all scores using matrix multiplication, which results in a horizontal distribution as shown in Figure 22. The uncontrolled variation due to repeat measurements has now been isolated to s_1. Therefore, it is now possible to disregard this score from subsequent MD calculations, as it no longer contains any useful information concerning the existence of notches.

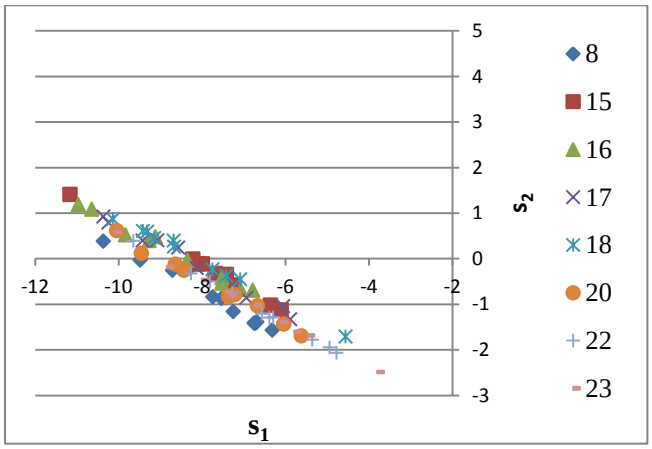

Figure 21: Plot showing an example of variation in repeat measurements due to horizontal probe off-centering.

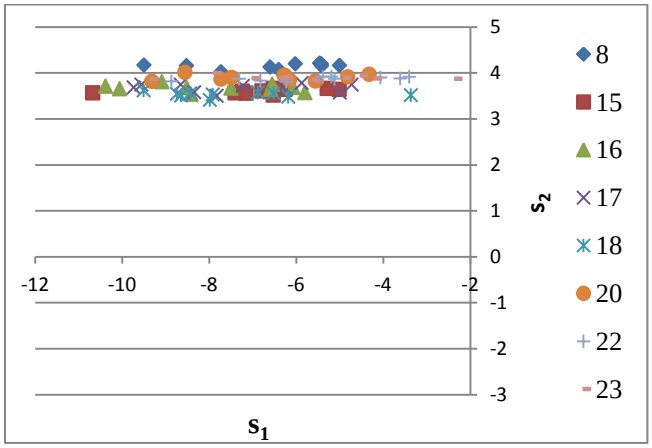

Figure 22: Plot showing an example of repeat measurement variation contained in s_1 only after a unitary rotation is applied.

5.6 Fastener Proximity to the Lap-Joint Edge

For the samples being evaluated, the proximity of each fastener to the lap-joint edge was observed to vary by up to +/- 1.8 mm. This variable distance from the lap-joint edge has an impact on the PEC signal, since the response of the pick-up coils due to the presence of the lap-joint edge changes as a function of distance from the edge. This relationship can be seen graphically by plotting any of the remaining blank scores (s_2 - s_5) with respect to edge distance. This relationship is shown for s_5 in Figure 23 while similar relationships for s_2 to s_4 are shown in Appendix A.

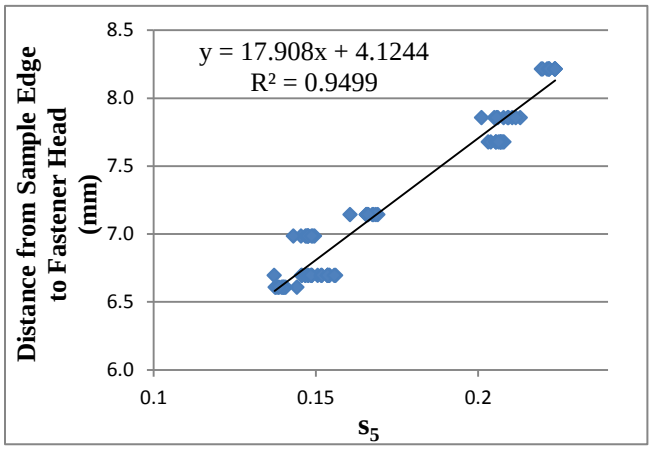

Figure 23: Fastener edge distance vs. s_5 for Standard 22 without edge correction.

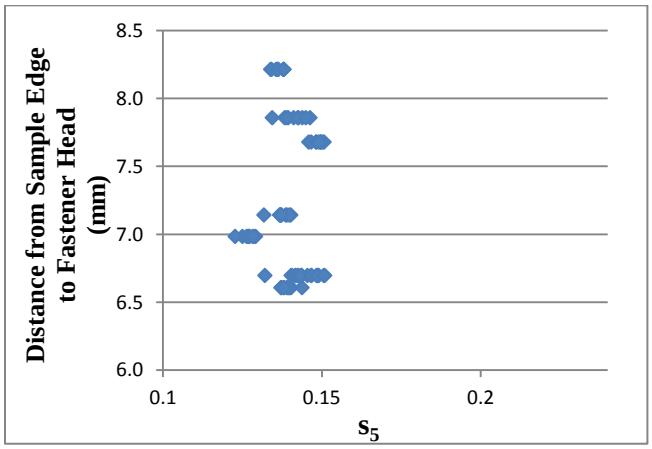

Figure 24**: Fastener edge distance vs. s_5 for Standard 22 after edge correction.**

For any of the remaining scores (s_2 - s_5) a linear relationship can be observed between the score and the proximity of the fastener to the lap-joint edge. The slope obtained from this relationship

can subsequently be used to apply a distance correction for each remaining score (s_2 - s_5) as depicted for s_5 in Figure 24. This distance correction effectively removes differences in score values due to variation in fastener proximity to the lap-joint edge. The removal of this edge effect also has a significant impact on compression of the blank cluster. Figure 25 shows the blank cluster for a plot of s_2 vs. s_3 using blank fastener data obtained from three NAVAIR standards prior to applying any edge correction. Once the edge corrections are applied, this cluster compresses as shown in Figure 26. This blank cluster compression is also shown in Appendix A for s_4 vs. s_5, s_2 vs. s_4 and s_2 vs. s_5.

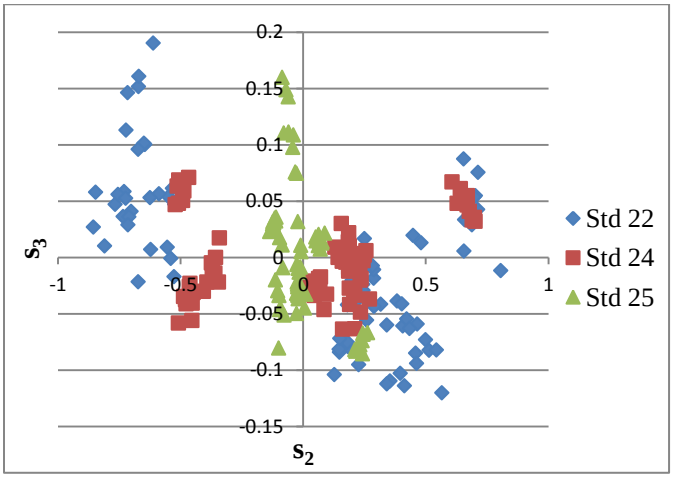

Figure 25: Plot of blank scores for three standards showing s_2 vs. s_3 without edge corrections.

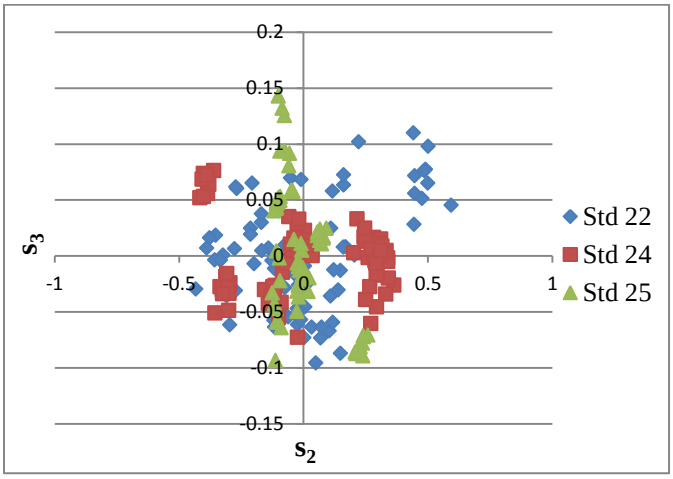

Figure 26: Plot of blank scores for three standards showing s_2 vs. s_3 after edge corrections.

5.7 Robust Statistics Simulations

For the analysis outlined in Section 5.3, determination of the MD requires that signal information related to blank fastener locations be known, as it is a Type 3 outlier detection method [16]. However, the use of a calibration standard is not possible in this application due to slight variations between sample skin thickness and interlayer gap as presented in Table 11. This is problematic in field applications as this information, which is required to generate the blank cluster, cannot be readily obtained. Thus, any deployable technique must have the ability to distinguish blindly between blanks and cracks without the use of a calibration standard. The robust statistics method known as smallest half volume (SHV) has been identified as a potential solution to this in-situ calibration issue [27]. Under the assumption that only a small fraction of those fastener locations scanned will contain defects, this analysis technique can be applied to obtain blind detection results with no prior knowledge of blank fastener locations [19].

As the samples used for this work were specifically engineered to have more notches than blanks, the assumption of more blanks than flawed sites is violated due to the large number of statistical outliers. Additionally, each evaluated NAVAIR sample only contains anywhere from seven to ten unflawed fastener sites. Previous work conducted by Underhill *et al*. [27] suggests that a minimum sample size of 40 blank fasteners is required to obtain reliable detection results for the inspection technique used for this thesis work. Thus, in order to artificially inflate the number of blank fastener measurements, covariance matrices that have statistically similar properties to real experimental measurements must be obtained. To achieve this, it is first necessary to generate random data with the same statistical distribution by using the technique described in Section 2.10. These randomly generated covariance matrices can now be used to simulate real world detection scenarios where only a small number of defects exist relative to the number of blanks. Both the cluster analysis and robust statistics methodologies can be evaluated using this simulation technique.

When combining this simulation technique with the SHV algorithm, an appropriate data fraction [19] must be chosen. This value, which is commonly 50% [16], is required to define what percentage of the data will be used in determining the statistical center, or in other words, it provides an estimate of the number of blanks in the sample. This value explicitly defines the fraction of data to be used in the construction of the covariance matrix. For example, a data

fraction of 90% means that the most tightly clustered 90% of the data is used for the purpose of constructing the covariance matrix. Previous work conducted by Underhill *et al.* [19] has concluded that for second layer crack detection, with a small number of outliers, the best detection performance is obtained when this value is set to 97.5%. This result was obtained based on a series of simulations conducted using a total of four randomly selected cracks and 40 blank measurements corresponding to approximately 10% outlier contamination in the data set. The simulations were repeated for different data fraction values with the resulting detection rates plotted as a function of false call rate. This plot produced by Underhill *et al*. [19] is shown in Figure 27.

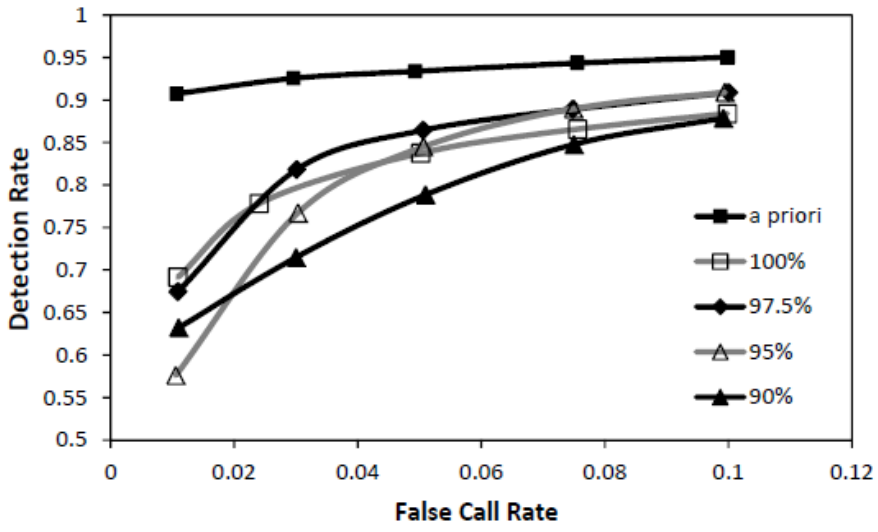

Figure 27: Detection rate vs. false call rate for simulations using the SHV algorithm with a data set containing 4 cracks and 40 blanks [19].

In this figure, the line labeled *a priori* represents results obtained when blank fastener information is known prior to analysis. Although the 10% outlier contamination chosen would suggest that a data fraction of 90% would produce the best results, this is not the case. From this figure, it can be clearly seen that choosing a data fraction of 90% produces the poorest results for the data fractions evaluated. When this data fraction is further increased, results seem to improve. However, the 100% data fraction produces detection results that are notably poorer than the case when the data fraction is set to 97.5%. This result demonstrates the robustness of the SHV algorithm, as results actually improve rather than degrade when some outliers are included in the data set used to determine the covariance matrix.

6. Results

6.1 General

This section presents the results obtained using measurements taken for the NAVAIR sample series described in Section 4.5, combined with the analysis approaches outlined in Section 5. First, results for the evaluation of four different pulsed eddy current (PEC) probes are presented. These results demonstrate how EDM notch detection is influenced by central driving coil core diameter and differential pick-up coil pair spacing. Next, results for the single sample detection case are presented for two different false call rates. This is followed by the results obtained by combining three samples and processing them as a single test case. Finally, simulation detection results are presented for cases when blank fastener locations are known and when no previous knowledge is known about the data set.

6.2 Probe Enhancement Results

Notch detection rates for each of the four probes are shown per fastener in Figure 28 for Probes 1, 2 and 4, and in Figure 29 for Probes 3 and 4. The results displayed in both of these figures are based on measurements taken from Standard 22, with a threshold value selected to obtain an 8% false call rate. The overall detection results for each probe are presented in Table 12. Due to immediate equipment availability, measurements were taken using the Darlington pair based amplification circuit described in Section 4.4. This transistor based amplification circuit did not provide the same detection capability as the op-amp based amplification circuit later employed, due to increased noise. However, the inferior performance of the transistor based amplification circuit did help to clearly identify which probe configuration would give the best detection results. Each data set collected consisted of five measurements per fastener. In order to most accurately represent real world conditions, single measurements were taken from fasteners 1 to 23 with this method repeated five times. The alternative method would be to measure a single fastener five separate times before moving onto the next fastener. A total of five data sets were collected for each probe configuration for a total of 575 measurements per probe. As notch orientations vary, each coil pair will have a different sensitivity to notch detection. For this reason, final notch detection results were achieved by recording a hit if a hit was obtained on any coil pair. The significance of these results will be discussed in greater detail in Section 7.1.

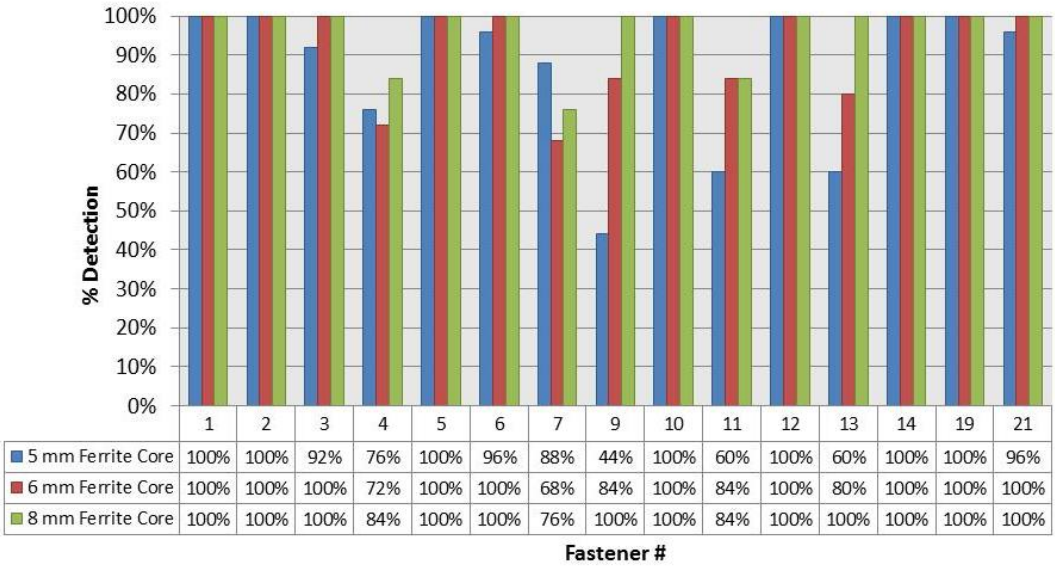

	1	2	3	4	5	6	7	9	10	11	12	13	14	19	21
5 mm Ferrite Core	100%	100%	92%	76%	100%	96%	88%	44%	100%	60%	100%	60%	100%	100%	96%
6 mm Ferrite Core	100%	100%	100%	72%	100%	100%	68%	84%	100%	84%	100%	80%	100%	100%	100%
8 mm Ferrite Core	100%	100%	100%	84%	100%	100%	76%	100%	100%	84%	100%	100%	100%	100%	100%

Figure 28: Side-by-side comparison of notch detection results for Probes 1, 2 & 4 with a total of 25 measurements taken per fastener.

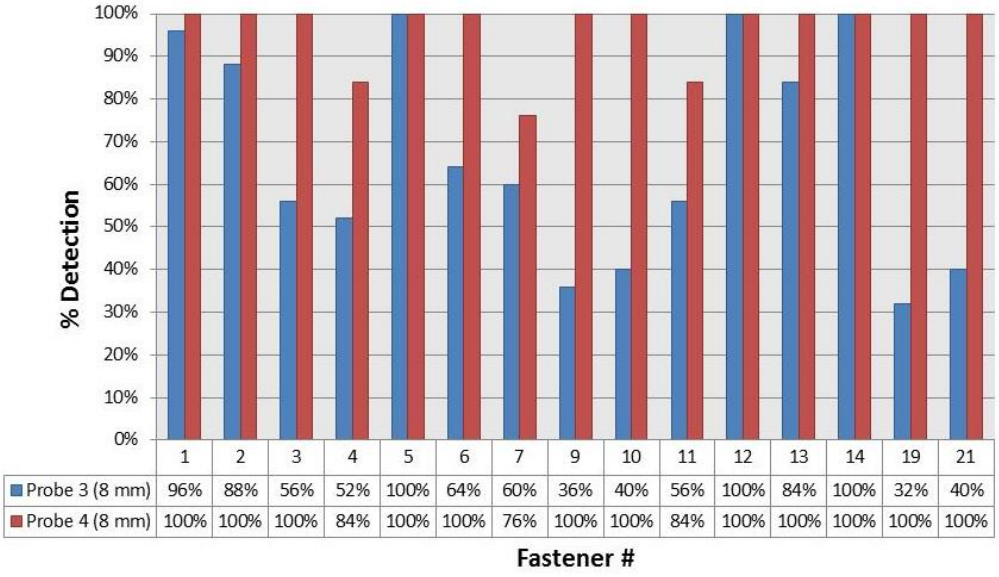

	1	2	3	4	5	6	7	9	10	11	12	13	14	19	21
Probe 3 (8 mm)	96%	88%	56%	52%	100%	64%	60%	36%	40%	56%	100%	84%	100%	32%	40%
Probe 4 (8 mm)	100%	100%	100%	84%	100%	100%	76%	100%	100%	84%	100%	100%	100%	100%	100%

Figure 29: Side-by-side comparison of notch detection results for Probes 3 & 4 with a total of 25 measurements taken per fastener.

Table 12: Overall detection results for Probes 1, 2, 3 and 4.

Probe	Detection Rate 8% False Call
Probe 1 (5 mm)	87%
Probe 2 (6 mm)	93%
Probe 3 (8 mm)	67%
Probe 4 (8 mm)	96%

6.3 Measurement Detection Results

6.3.1 Single Sample Detection Results

For the single sample detection cases, the MD data matrix **X** was determined using only blank scores from the individual sample being evaluated. Measurements were taken using the improved op-amp based amplification circuit paired with Probe 4, the top performing probe configuration assessed. Only one data set was collected for each sample. Single measurements were taken for each fastener and the measurements were repeated a total of ten times. In this case, detection results were obtained without applying any rotation to the scores and without applying any distance-to-edge correction. A summary of the results obtained for the single sample detection cases, with consistent false call rates of 5% and 10%, along with the notch size corresponding to the largest miss, are presented in Table 13. These results will be discussed in greater detail in Section 7.2.

Table 13: Summary of single sample detection results.

Sample ID	Detection Rate 5% False Call	Largest Miss 5% False Call	Detection Rate 10% False Call	Largest Miss 10% False Call
Standard 22	99%	0.89 mm	99%	0.89 mm
Standard 23	81%	2.16 mm	86%	2.16 mm
Standard 24	95%	0.89 mm	99%	0.89 mm
Standard 25	95%	1.27 mm	96%	0.76 mm
Standard 26	87%	2.16 mm*	89%	2.16 mm*
Standard 28	81%	2.79 mm	91%	1.91 mm
Standard 32	84%	1.91 mm	87%	1.91 mm
Average	89%		92%	

***** Only occurs for 10% of measurements taken at this flaw location. The largest significant miss occurring >10% of the time is 1.65 mm for both false call rates given.

6.3.2 Combined Sample Detection Results

In this section, standards 22, 24 and 25 were evaluated as a combined sample set. These standards were chosen based on similarities in sheet thickness and interlayer gap. The results obtained for the single sample case were also considered in this selection process. For this combined sample detection case, the MD data matrix **X** was determined using the combined blank scores from these three samples. A single data set was collected for each of the three samples and measurements were taken using the improved op-amp based amplification circuit paired with Probe 4. A total of ten repeat measurements were recorded for each fastener. For each standard, measurements were conducted at different times and as such were subject to the environmental shifts described in Section 5.4. For this combined case, detection results were initially obtained by removing only the environmental shift, without applying any rotation to the scores and without applying any distance-to-edge correction. These detection results were then re-evaluated by applying the score rotations and distance corrections described in Sections 5.5 and 5.6. A summary of the results obtained for the combined sample detection case, with consistent false call rates of 5% and 10%, along with the notch size corresponding to the largest miss, are presented in Table 14. These results will be discussed in greater detail in Section 7.2.

Table 14: Summary combined sample detection results.

Sample ID	Detection Rate 5% False Call	Largest Miss 5% False Call	Detection Rate 10% False Call	Largest Miss 10% False Call
No Rotation and No Correction	77%	3.30 mm	79%	3.30 mm
Rotated and Corrected	93%	3.30 mm	95%	3.30 mm

6.4 Simulation Detection Results

Using the simulation technique described by Underhill *et al.* [19] [27], as outlined in Section 5.7, a number of statistical simulations were performed using randomly generated statistical data. This randomly generated data was derived from real data collected for the purpose of the single sample detection case. This data was further post-processed in order to remove effects due to environmental conditions, repeat measurements and fastener proximity to lap-joint edge using the techniques outlined in Sections 5.4 to 5.6.

6.4.1 Results Obtained with Known Blanks

For this section, the MD data matrix **X** was determined for each individual sample being evaluated using randomly generated blank fasteners. The blank fastener scores were randomly generated from real blank data using the technique describe previously in Section 2.10. For each run of the simulation, a total of 40 randomly generated blanks were selected along with randomly selected measurement data from four real notches. A total of 200 runs were conducted. The results obtained for a consistent 5% false call rate are presented in Table 15. These results will be discussed further in Section 7.2.

Table 15: Summary of detection results for known randomly generated blanks.

Sample ID	Detection Rate 5% False Call
Standard 22	100%
Standard 24	100%
Standard 25	100%

If the false call rate is further reduced below 5%, then these detection results can also be expected to decrease. Table 16 shows the minimum false call rates for each sample where a miss occurs.

Table 16: Minimum false call rate where miss occurs.

Sample ID	False Call Rate for Miss
Standard 22	0.2%
Standard 24	0.0%
Standard 25	0.9%

6.4.2 Blind Detection Results

For this section, the SHV algorithm was used without indication of which data points were randomly generated blanks and which were taken from real notch data. For each run of the simulation, a total of 40 randomly generated blanks were selected along with randomly selected measurement data for four real notches. For reasons outlined in Section 5.7, a data fraction of 97.5% was selected and a total of 200 runs of the simulation algorithm were conducted. A summary of the results obtained for the SHV detection case for consistent false call rates of 5% and 10% are presented in Table 17. These results will be discussed further in Section 7.2.

Table 17: Summary of detection results for SHV in the presence of outliers.

Sample ID	Detection Rate 5% False Call	Detection Rate 10% False Call
Standard 22	99%	99%
Standard 24	99%	100%
Standard 25	99%	99%

7. Discussion

7.1 Probe Enhancement

From the results shown in Figure 28, it can be seen that notch detection improves as the probe driving coil ferrite core diameter increases relative to the ferrous fastener head size. Fasteners #9 and #13 are 1.52 mm second layer notches with results that clearly illustrate this improvement in detection rate. It is also important to note that the detection of the 0.89 mm notches at Fasteners #4 and #11 also show improved detection with increase in ferrite core diameter. This is significant as both of these notches represent second layer cracks growing towards the bottom layer edge, which is a direction of structural concern. This result is consistent with the outcome postulated by Whalen [2], as discussed in Section 3.4.

It can be observed in Figure 29 that a decrease in differential pick-up coil pair spacing from 16.0 mm to 14.7 mm will result in a significant increase in the rate of notch detection. As a result of using a ferrous fastener to act as a conduit for magnetic flux, the PEC probe utilized in this research concentrates the magnetic field and intensifies the resulting eddy currents in the aluminum surface near the fastener. As such, moving the pick-up coils closer to the driving coil and the edge of the fastener is expected to yield a better pick-up coil response and defect detection rate, as demonstrated. It is also important to note the poor detection of Fastener #7, which from Table 3, is a 2.03 mm second layer notch orientated in the 270° direction. As this notch is located in the bottom layer of the sample, the notch orientation is in the direction of greatest material width as it is orientated away from the edge of the bottom layer and towards the top edge of the sample. With greater width of material in this direction, currents are able to move more freely and are not confined due to the edge of the bottom layer or adjacent fasteners. Consequently, the current density may be lower on this side of the fastener, thus decreasing detectability.

7.2 Selecting an Analysis Method

From the results displayed in Table 13 for the single sample cases, it has been shown that a high level of detection can be achieved without any manipulation of the scores obtained from the

MPCA. While the most desirable results are obtained from standards 22, 24 and 25, there are apparent detection problems with the remaining standards. First, Standard 23 has a much lower detection rate than anticipated with a largest miss of 2.16 mm for a 5% false call rate. This loss of detection can be attributed to the fact that this sample has a larger nominal gap than the other samples considered. Previous work by Pan *et al* [33] and Giguère *et al*. [39] suggests that it should be possible to compensate for lift-off (additional space present between the probe and sample being inspected) effects present due to variation in gap when using the PEC technique. However, this was not investigated in this thesis. Standard 26 has a largest miss of 2.16 mm for 10% of measurements taken at this flaw location given a 5% false call rate. However, the largest significant miss (a miss that occurs greater than 10% of the time for a given notch size) is actually 1.65 mm for the same false call rate. This lower detection for Standard 26 can be attributed to the fact that both the top and bottom layers of this sample are nominally thicker when compared with the remainder of NAVAIR standards. This increase in thickness, especially in the top layer, implies that a greater depth of penetration is required in order to detect the second layer notches. The loss of detection for Standard 28, which has a largest miss of 2.79 mm, can be attributed to the proximity of fasteners to the lap-joint edge. For this standard, the majority of fasteners are placed closer to the lap-joint edge by an average of 1 mm, which intensifies the edge effect discussed in Section 5.6. This sample also has the largest differences in fastener-to-edge distance noted for a single sample. As a result of these differences, the blank fastener cluster is more spread out, resulting in more data points representing notches being contained within the boundary of the blank cluster. This spread in the blank cluster is still apparent even after the distance corrections have been applied, which suggests that there is a limit to how much variation can be accounted for when using the distance-to-edge correction method detailed in Section 5.6. Similar to Standard 23, Standard 32 has a larger nominal gap when compared to other standards in the sample series. This, combined with the fact that the sample has a thicker bottom sheet and notable surface damage, provides some explanation for the reduced notch sensitivity and the 1.91 mm largest miss for a false call rate of 5%.

When three samples are combined, the detection rate is substantially reduced even though the same analysis method is applied. This loss of detection can be attributed partially to not accounting for repeat measurement effects and differences in fastener proximity to the lap-joint edge. Once corrections have been applied to account for these variables, the detection rate for

the combined sample case significantly improves to a detection level that is comparable to the single sample cases. For the improved combined sample case there is a largest recorded miss of 3.30 mm for a 5% false call rate. This loss of sensitivity to larger notches suggests that, in the combined sample case, there are additional variables impacting notch detection which are not being accounted for, such as top and bottom sheet thickness, and interlayer gap. The detection methodologies presented in this thesis work rely heavily on the assumption that fasteners with notches present will appear as outliers in the data set. The analysis processes look for all outliers in the measurement data under the assumption that signal differences due to the presence of notches will be more influential than those signal differences resulting from other variables. This is the same assumption presented by Annis [40], who suggests that the single most influential factor is nearly always the target (notch) size. However, if other variables such as sheet thickness and interlayer gap are not appropriately accounted for in the analysis procedure, then notch sensitivity can be lost when combining samples. When these additional essential parameters are not accounted for, then the outlying scores observed may not be representative of fastener sites with defects present. Therefore, an increase in false call rate would be required in order to maintain the desired level of detection.

The proposed cluster analysis method that only uses the MD as the classifier is a Type 3 outlier detection method and thus information about the blanks must be known in order to properly classify the data. For simulations using this method, 100% of notches as small as 0.76 mm (0.030”) could be detected for a 5% false call rate. However, to use this method in a field application, a calibration sample containing multiple blank faster locations would be required in order to define the blank cluster. This is problematic as it has been demonstrated in Section 6.3.2 that difficulties may arise when combining samples. Therefore, the use of data obtained from one sample (calibration standard) for the basis of classification of another sample (aircraft structure) may not be a possible solution.

Alternatively, the SHV approach is a Type 1 outlier detection method and thus no prior information about the sample is needed in order to classify the data. For simulations using this method, a 99% detection rate was achieved for three independent samples for a 5% false call rate. This 1% loss in detection is negligible given that this method is capable of self-calibrating without a reference sample. However, to use this method in a field application, the assumption that there are more blank fastener sites than sites containing cracks must hold true. As the

number of defects in the sample increases, the tightest cluster determined by the SHV algorithm will become more contaminated by outliers, resulting in a shift of the computed centroid. This will result in more outliers contained within the bounds of the blank cluster, leading to a decrease in defect detectability

7.3 Determining Detectable Flaw Size and False Call Rate

To uphold airworthiness requirements, a minimum detectable flaw size ($a_{90/95}$) as defined in Section 1.1, must be determined before this technique can be deployed for field application. Traditionally, the value of this reliability metric would be determined by producing a probability of detection (POD) curve [40]. However, as indicated by Aldrin *et al.* [41], current standard practices used for evaluation of measurement system capability may present limitations when applied to the assessment of NDT performance. One major obstacle is obtaining adequate experimental data to demonstrate and validate the technique [41]. Due to difficulties in obtaining a large number of samples, there is a growing tendency to reduce sample sizes, which consequently increases the uncertainty associated with the resulting POD curve [40]. Subsequently, the generation of a POD curve assumes that the most influential parameter is target (flaw) size [40]. This is a fair assumption for traditional ET where an operator observes the signal resulting from a flaw and correlates the measured amplitude to its size. However, in the case of PEC detection in the presence of ferrous fasteners, the extraction of essential parameters becomes more complex as the PEC technique has a heightened sensitivity to multiple variables. To determine a true minimum detectable flaw size ($a_{90/95}$), other essential parameters, not related to the size of the flaw, must first be identified and accounted for. This is essential in order to mitigate the influence of any uncontrolled parameters that may impact flaw detection sensitivity such as temperature, fastener-to-edge distance and interlayer gap. This influence of uncontrolled essential parameters, combined with a limited number of samples, suggests that a traditional hit/miss POD study may not be the optimal approach for determining minimum detectable flaw size ($a_{90/95}$) for this technique.

Both the cluster analysis approach and SHV methodologies use a selected threshold in order to determine if a flaw is present or not. Therefore, when the value of this threshold is decreased, flaw detection is improved. However, decreasing the threshold value consequently increases the

false call rate. Determination of an acceptable false call rate for this inspection technique is somewhat subjective as the consequence of a false call does not need to be as costly as it is with other techniques. Keeping in mind that the current inspection method of bolt hole eddy current (BHEC) requires removal of all fasteners in order to perform an inspection, the PEC inspection technique could simply be employed as a method of selective scanning. With this application, a PEC scan would be conducted in order to determine which fasteners to remove. Once removed, the hole could be scanned using BHEC in order to gather more information about the defect. This provides validation of the call made by the PEC system and implies that the true consequence of a false call in this scenario may have no safety implications. Additionally, a great deal of time, cost and human resources are saved by only having to remove a select number of fasteners instead of removing them all. Consequently, the risk of collateral damage is mitigated.

8. Summary and Future Work

8.1 Summary

Pulsed eddy current (PEC) is a NDT technique currently being investigated as a viable method of detecting cracks due to cyclic loading in multi-layered wing structure without ferrous fastener removal. During PEC inspection, the fastener is used as a conduit for the magnetic flux created by the driving coil, which allows for a deeper penetration of eddy currents. It has been hypothesized that an increase in driving coil ferrite core size relative to the fastener head will produce a greater depth of penetration, resulting in an increased probability of crack detection. It has been established that defect detectability in multi-layer structures can be greatly impacted by a number of essential parameters such as temperature, probe off-centering, distance to the lap-joint edge and interlayer gap.

In order to explore the effects of probe characteristics on crack detection, leading towards probe and analysis enhancement for second layer crack detection, numerous measurements were performed using a series of samples representative of the wing structure of a CP-140 Aurora (P-3 Orion) aircraft. A total of four probes were considered in order to evaluate the effects of driving coil ferrite core diameter and differential pick-up coil pair spacing on defect detection rates. All data was post-processed using a modified principle components analysis (MPCA) and graphical results were generated for each probe configuration. It was determined from the probe enhancement results that a larger driving coil ferrite core probe will produce better detection results when compared to a probe with a smaller driving coil ferrite core for similar pick-up coil pair spacing. However, this correlation between driving coil ferrite core diameter and defect detection is not expected to continue indefinitely as the ferrite core diameter is further increased. The methods of defect detection presented in this thesis rely on the fact that the ferrous fastener acts as a flux conduit, which amplifies the magnetic field and carries it to greater depths, thereby enhancing the resulting eddy currents encircling the fastener. For this reason, it is advantageous to position the pick-up coils as close to the center of the probe as possible in order to generate a better pick-up coil response. Further increasing the driving coil ferrite core diameter relative to the ferrous fastener head diameter will result in the pick-up coils being moved further away from the area of magnetic flux concentration and associated eddy current density. Therefore, the rate

of defect detection is expected to fall off when the driving coil ferrite core diameter is much larger than the ferrous fastener head diameter due to an increase in pick-up coil pair spacing as shown by the comparison of Probes 3 and 4 in Section 6.2.

An enhanced analysis approach for detecting second layer notches in multiple CP-140 Aurora (P-3 Orion) lap-joint samples was also presented. The essential parameters investigated included shifts due to environmental factors such as uncontrolled temperature, repeat measurement effects due to probe off-centering and fastener proximity to the lap-joint edge. Using these analysis enhancements, it was possible to combine multiple CP-140 Aurora (P-3 Orion) samples with notch detection results similar to those obtained for single sample cases. However, it was noted that multiple problems can arise when not all of the essential parameters are accounted for, as the results obtained can also be impacted by differences in physical characteristics of the samples, such as layer thickness and interlayer gap.

Finally, a series of simulations was performed in an effort to develop a Type 1 blind detection capability for inspection of CP-140 Aurora lap-joint structures. The SHV algorithm that was used works under the assumption that only a small number of cyclic fatigue cracks exist at bore hole locations relative to the total number of inspected fastener sites. In order to validate the employed simulation technique, results were also generated for the Type 3 cluster analysis approach where blank fastener locations must be known. A comparison of the results obtained from both outlier detection approaches shows that negligible detection capability was lost when the information about blank fastener signals was not known during data post-processing. Therefore, the results presented in this thesis work suggest that self-calibrating blind detection of cyclic fatigue cracks in second layer wing structure is possible in the presences of ferrous fasteners without prior knowledge of the sample under test and without the use of costly calibration standards.

8.2 Future Work

Based on the findings of this thesis work, the following work is recommended for development of a reliable field deployable technique:

- Establish a relationship between the confidence bounds of the multivariate analysis approaches used for this PEC technique and those of a classical hit/miss POD.
- Develop improved methods of comparing and combining multiple samples since layer thickness and interlayer gap may cause shifts and rotations in the blank cluster, leading to loss of detectability.
- Further enhance PEC analysis methods for separation of top and bottom layer cracks.
- Further enhance PEC analysis methods for determination of crack size and orientation.
- Conduct field trials of the inspection technique to confirm that lab results can be reliably duplicated when the technique is applied to in-service aircraft structures.
- Develop a deployable field kit that includes a robust probe design along with a user-friendly software interface capable of post-processing the measurement data.

References

[1] J. R. Evans and W. M. Lindsay, Managing for Quality and Performance Excellence, Mason: South-Western, 2008.

[2] N. E. Dowling, Mechanical Behavior of Materials, Upper Saddle River: Pearson Education Inc., 2013.

[3] D. E. Bray and R. K. Stanley, Nondestructive Evaluation: A Tool for Design, Manufacturing and Service (Revised Edition), Boca Raton: CRC Press, 1997.

[4] A. Fahr, Aeronautical Applications of Non-destructive Testing, Lancaster: DEStech Publications Inc., 2014.

[5] Department of Defense, "Nondestructive Inspection Methods, Basic Theory," Department of Defense, 2007.

[6] European Network for Inspection and Qualification, "ENIQ Recommended Practice 1: Influential / Essential Parameters," European Communities, 2005.

[7] D. Broek, The Practical Use of Fracture Mechanics, Dordrecht: Kluwer Academic Publishers, 1989.

[8] C. A. Stott, P. R. Underhill and T. W. Krause, "Pulsed Eddy Current Detection of Cracks in Multilayer Aluminum Lap Joints," *IEEE Sensors Journal,* vol. 15, pp. 956-962, 2015.

[9] H. Lemire, P. R. Underhill, T. W. Krause, M. Bunn and D. J. Butcher, "Improving Probability of Detection of Bolt Hole Eddy Current Inspection," *Research in Nondestructive Evaluation,* vol. 21, pp. 1-16, 2010.

[10] Department of Defense, Nondestructive Evaluation System Reliability Assessment, MIL HDBK 1823A, Department of Defense, 2009.

[11] C. Stott, "Pulsed Eddy Current Inspection of Second Layer Wing Structure," M.A.Sc. thesis, Department of Chem. and Chem. Eng., RMCC, Kingston, 2014.

[12] P. P. Whalen, "Transient Eddy Current Inspection in the Presence of Ferrous Fasteners in Multi-Layered Aluminum Structures," M.A.Sc. thesis, Department of Chem. and Chem. Eng., RMCC, Kingston, 2010.

[13] T. W. Krause, C. Mandache and J. H. Lefebvre, "Diffusion of Pulsed Eddy Currents in Thin Conducting Plates," *American Institute of Physics*, vol. 975, pp. 368-375, 2008.

[14] V. Hodge and J. Austin, "A survey of outlier detection methodologies," *Artificial Intelligence Review*, vol. 22, no. 2, pp. 85-126, 2004.

[15] V. Barnett and T. Lewis, Outliers in Statistical Data, New York: John Wiley & Sons, 1994.

[16] W. J. Egan and S. L. Morgan, "Outlier Detection in Multivariate Analytical Chemical Data," *Analytical Chemistry*, vol. 70, no. 11, pp. 2372-2379, 1998.

[17] J. Lattin, J. D. Carroll and P. E. Green, Analyzing Multivariate Data, Pacific Grove: Brooks/Cole, 2003.

[18] P. F. Horan, P. R. Underhill and T. W. Krause, "Real Time Pulsed Eddy Current Detection of Cracks in F/A-18 Inner Wing Spar Using Discriminant Separation of Modified Principal Components Analysis Scores," *IEEE Sensors*, vol. 14, no. 1, pp. 171-177, 2014.

[19] P. R. Underhill, D. Butt and T. W. Krause, "Blind Detection of Cracks at Fasteners in CP-140 Aircraft Using Pulsed Eddy Current," *19th World Conference on Non-Destructive Testing*, 2016.

[20] J. D. Griffiths, Introduction to Electrodynamics, Upper Saddle River: Prentice-Hall, 1999.

[21] H. D. Young and R. A. Freedman, University Physics, San Francisco: Pearson Education, 2004.

[22] G. Rizzoni, Principles and Applications of Electrical Engineering, New York: McGraw-Hill, 2007.

[23] S. Goldman, Transformation Calculus and Electrical Transients, New York: Prentice Hall Inc., 1949.

[24] D. R. Desjardins, T. W. Krause and L. Clapham, "Transient response of a driver-pickup probe in transient eddy current testing," *NDT & E International*, vol. 75, pp. 8-14, 2015.

[25] P. Horan, P. Underhill and T. W. Krause, "Pulsed eddy current detection of cracks in F/A-18 inner wing spar without wing skin removal using Modified Principal Components Analysis," *NDT&E International*, vol. 55, pp. 21-27, 2013.

[26] P. J. Rousseeuw and M. Hubert, "Robust statistics for outlier detection," *Wiley Interdisciplinary Reviews: Data Mining and Knowledge Discovery,* vol. 1, no. 1, pp. 73-79, 2011.

[27] P. R. Underhill, C. Stott and T. W. Krause, "In-Situ Calibration of Pulsed Eddy Current Detection of Cracks at Fasteners in CP-140 Aircraft," *Review of Progress in Quantitative Nondestructive Evaluation,* vol. 1706, pp. 090004-1 to 090004-8, 2016.

[28] S. C. Chapra and R. P. Canale, Numerical Methods for Engineers, Montreal: McGraw-Hill, 1988.

[29] V. B. Wwedensky, "Concerning the eddy currents generated by a spontaneous change of magnetization," *Annalen de Physik,* vol. 64, pp. 609-620, 1921.

[30] D. Desjardins, "Analytical Modeling for Transient Probe Response in Eddy Current Testing," RMC, Kingston, 2011.

[31] R. C. Callaroti, P. Schmidt and H. Arqué, "Theory of the Measurement of Thickness and Conductivity of Cylindrical Shells by an Inductive Method," *Journal of Applied Physics,* vol. 43, no. 10, pp. 3952-3958, 1972.

[32] Y. He, M. Pan, D. Chen and F. Luo, "PEC defect automated classification in aircraft multi-ply structures with interlayer gaps and lift-offs," *NDT&E International,* vol. 53, pp. 39-46, 2013.

[33] M. Pan, Y. He, G. Tian, D. Chen and F. Luo, "PEC Frequency Band Selection for Locating Defects in Two-Layer Aircraft Structures With Air Gap Variations," *Transactions on Instrumentation and Measurement,* vol. 62, no. 10, pp. 2849-2856, 2013.

[34] Y. He, M. Pan , F. Luo, D. Chen and X. Hu, "Support vector machine and optimised feature extraction in integrated eddy current instrument.," *Measurement,* vol. 46, pp. 764-774, 2013.

[35] D. R. Desjardins, G. Vallieres, P. P. Whalen and T. W. Krause, "Advances in Transient (Pulsed) Eddy Current For Inspection of Multi-Layer Aluminum Structures in the Presence of Ferrous Fasteners," *Review of Progress in Quantitative Nondestructive Evaluation,* vol. 1430, pp. 400-407, 2012.

[36] V. K. Babbar, P. R. Underhill, C. Stott and T. W. Krause, "Finite Element Modeling of Second Layer Crack Detection in Aircraft Bolt Holes with Ferrous Fasteners Present," *NDT&E International,* vol. 65, pp. 64-71, 2014.

[37] "Dual Power Operational Amplifers - PA75," APEX Microtechnology Inc., Tucson, 2012.

[38] J. A. Buck, P. R. Underhill, J. E. Morelli and T. W. Krause, "Simultaneous Multiparameter Measurement in Pulsed Eddy Current Steam Generator Data Using Artificial Neural Networks," *IEEE Transactions on Instrumentation and Measurement,* vol. 65, no. 3, pp. 672-679, 2016.

[39] S. Giguère, B. A. Lepine and J. M. S. Dubois, "Pulsed Eddy Current Technology: Characterizing Material Loss with Gap and Lift-off Variations," *Research in Nondestructive Evaluation,* vol. 13, no. 3, pp. 119-129, 2001.

[40] P. E. Annis, "Influence of Sample Characteristics on Probability of Detection Curves," *Review of Progress in Quantitative Nondestructive Evaluation,* vol. 1581, pp. 2039-2046, 2014.

[41] J. C. Aldrin, C. Annis, H. A. Sabbagh, J. S. Knopp and E. A. Lindgren, "Assessing the Reliability of Nondestructive Evaluation Methods for Damage Characterization," *Review of Progress in Quantitative Nondestructive Evaluation,* vol. 1581, pp. 2071-2078, 2014.

Appendix A

Additional plots showing the relationship between fastener proximity to the lap-joint edge and scores s_2 to s_4 are shown in Figures 30 to 35. Additional plots showing the impact of the distance corrections described in Section 5.6 on compression of the blank scores for s_4 vs. s_5, s_2 vs. s_4 and s_2 vs. s_5 are shown in Figures 36 to 41.

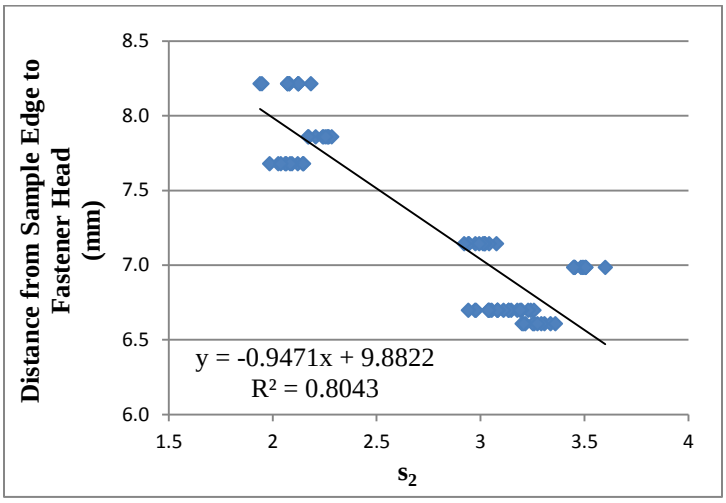

Figure 30: Fastener edge distance vs. s_2 for Standard 22 without edge correction.

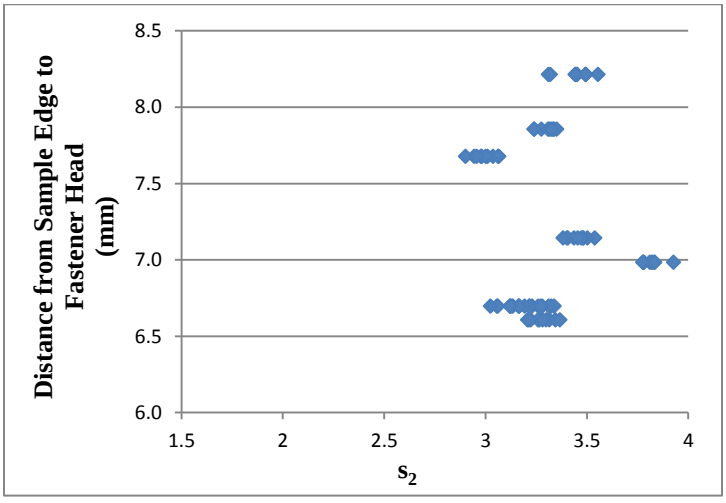

Figure 31: Fastener edge distance vs. s_2 for Standard 22 after edge correction.

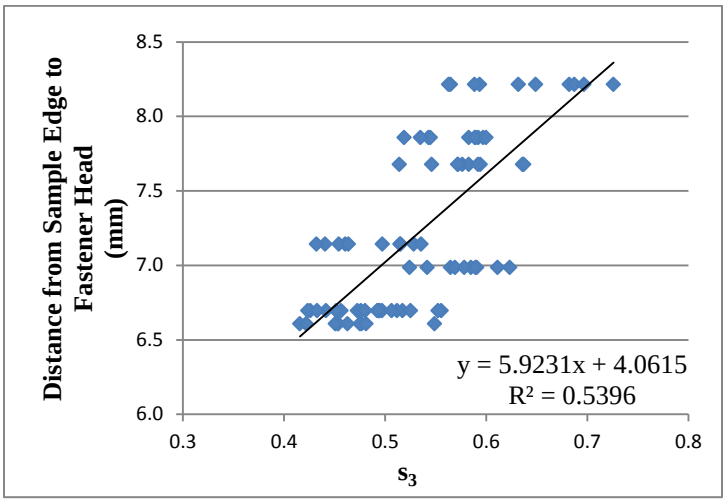

Figure 32: Fastener edge distance vs. s_3 for Standard 22 without edge correction.

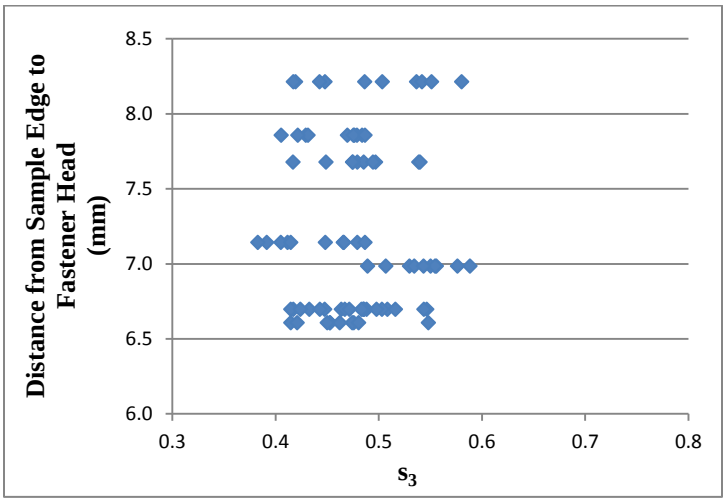

Figure 33: Fastener edge distance vs. s_3 for Standard 22 after edge correction.

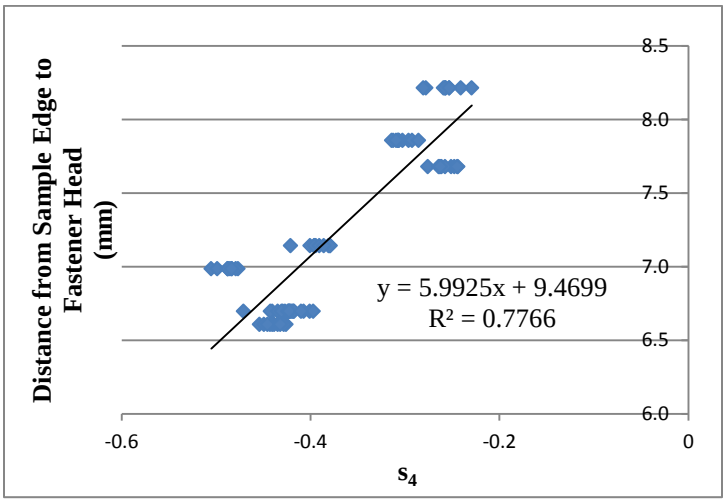

Figure 34: Fastener edge distance vs. s_4 for Standard 22 without edge correction.

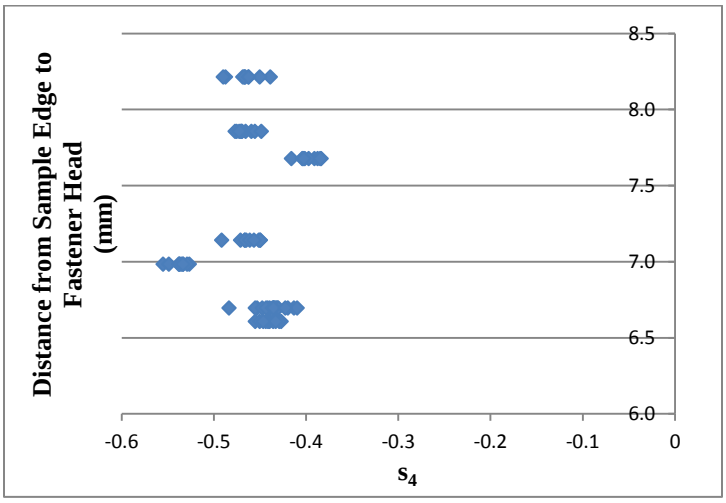

Figure 35: Fastener edge distance vs. s_4 for Standard 22 after edge correction.

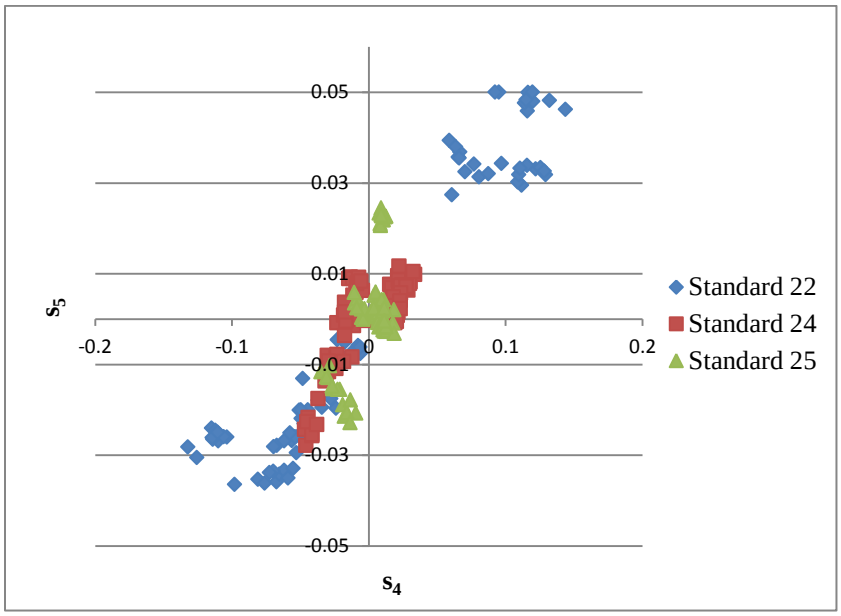

Figure 36: Plot of blank scores for three standards showing s_4 vs. s_5 without edge corrections.

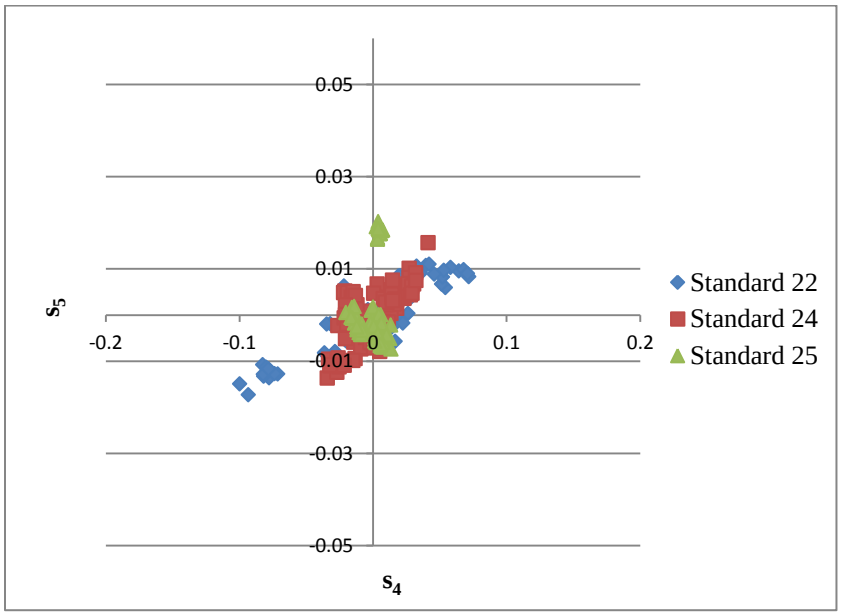

Figure 37: Plot of blank scores for three standards showing s_4 vs. s_5 after edge corrections.

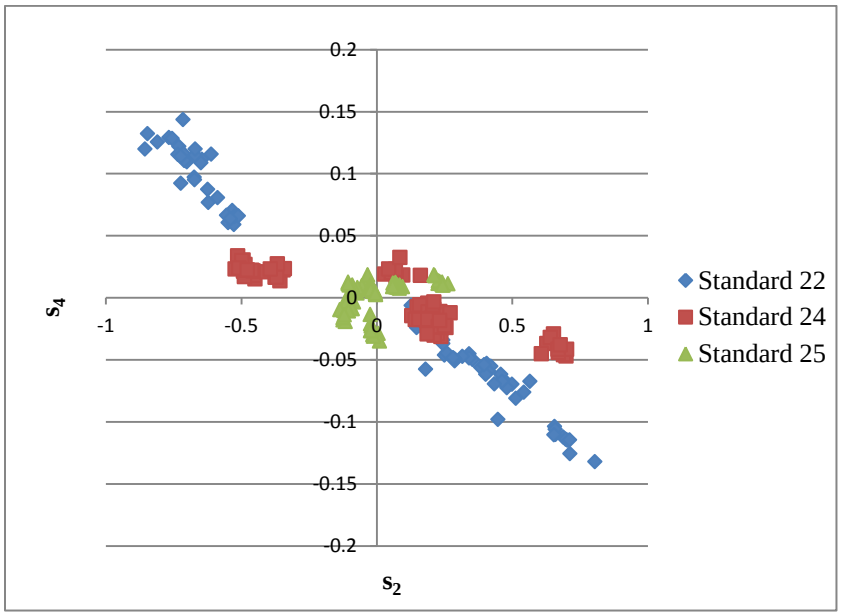

Figure 38: Plot of blank scores for three standards showing s_2 vs. s_4 without edge corrections.

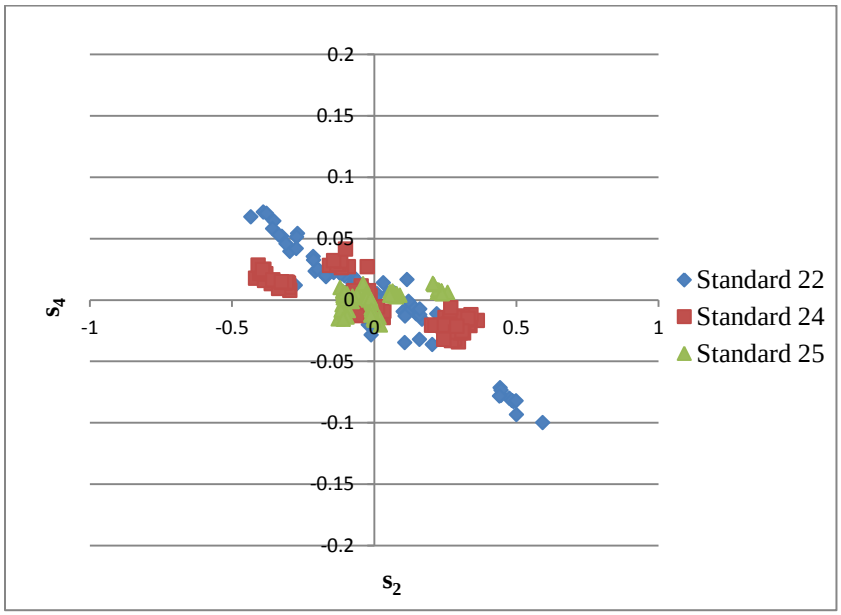

Figure 39: Plot of blank scores for three standards showing s_2 vs. s_4 after edge corrections.

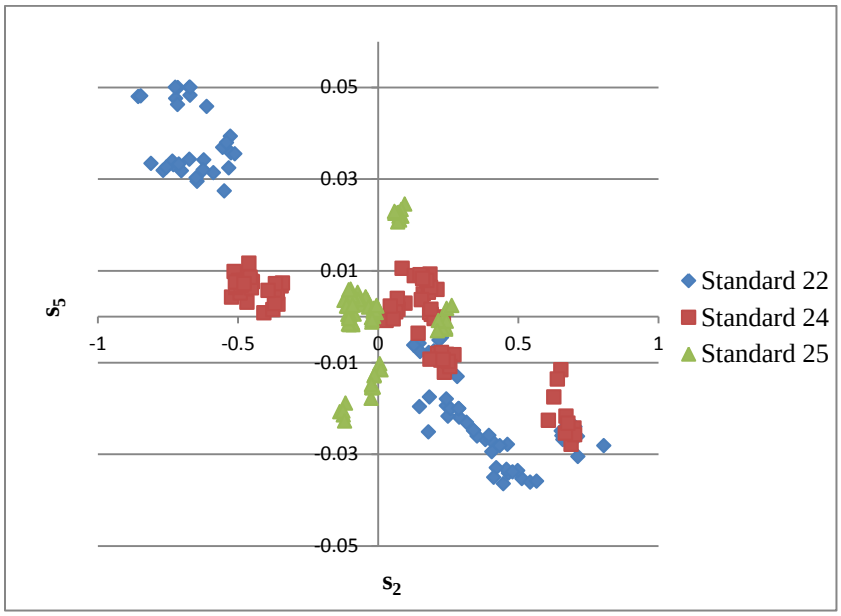

Figure 40: Plot of blank scores for three standards showing s_2 vs. s_5 without edge corrections.

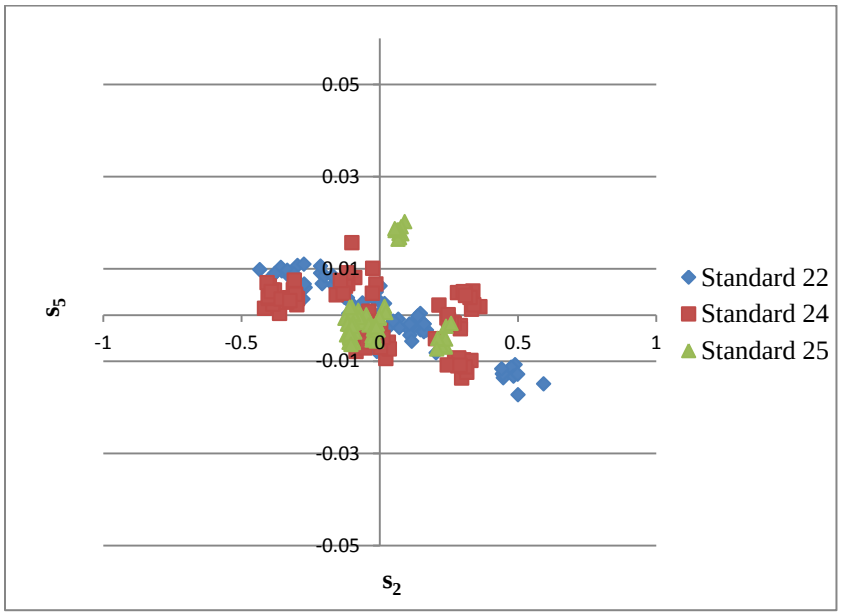

Figure 41: Plot of blank scores for three standards showing s_2 vs. s_5 after edge corrections.

Curriculum Vitae

Captain Dennis Morgan Butt was born in St. John's, Newfoundland on 6 September 1987. He obtained a Bachelor of Engineering (Mechanical) from the Department of Engineering and Applied Science at Memorial University of Newfoundland in May 2011. Upon graduation, he attended the Aerospace Engineering Officer Basic Course (AOBC) in Borden, Ontario. In 2012, he was posted to the Aerospace Engineering Test Establishment (AETE) in Cold Lake, Alberta. There, he served as a Flight Test Instrumentation Engineer responsible for the design and analysis of aircraft structural modifications required for the installation of data acquisition systems in support of flight test activities.

In 2014, upon completing his tour in Cold Lake, Captain Butt was posted to Kingston, Ontario to complete a Master of Applied Science in Chemical and Materials Engineering at the Royal Military College of Canada. While in Kingston, Captain Butt also completed the course requirements to obtain a Master of Technology Management from the Fisheries and Marine Institute of Memorial University of Newfoundland. This degree will be awarded June 2016.

Articles Published in Referred Journals/Books

D.M. Butt, P. R. Underhill and T. W. Krause, "Enhancing Pulsed Eddy Current for Inspection of P-3 Orion Lap-Joint Structures," *Review of Progress in Quantitative Nondestructive Evaluation*, Minneapolis, MN, USA, 26-31 July, 2015.

Conference Proceedings

P. R. Underhill, D. Butt and T. W. Krause, "Blind Detection of Cracks at Fasteners in CP-140 Aircraft Using Pulsed Eddy Current," *19th World Conference on Non-Destructive Testing*, Munich, Germany, June 13-17, 2016.

D.M. Butt, P.R. Underhill and T.W. Krause, "Pulsed Eddy Current Detection of Second Layer Cracks at Ferrous Fasteners in Aircraft Lap-Joint Structures," *19th World Conference on Non-Destructive Testing*, Munich, Germany, June 13-17, 2016.

Invited Talks and Papers Presented at Major Conferences and Symposia

D.M. Butt, P.R. Underhill and T.W. Krause, "Application of Pulsed Eddy Current for Inspection of CP-140 Lap-Joints," *Invited Talk at the RCAF NDT Seminar*, Trenton, ON, April 28, 2016.

D. M. Butt, P. R. Underhill and T. W. Krause, "Optimizing Pulsed Eddy Current Probes for Inspection of CP-140 Aurora Lap-Joints," *NDT in Canada Conference*, Edmonton, AB, June 15-17, 2015.